Evaluation of Single Event Effects Using the Ultrafast Pulsed Laser Facility at the Saskatchewan Structural Sciences Centre

A Thesis Submitted to the
College of Graduate Studies and Research
in Partial Fulfillment of the Requirements
for the Degree of Master of Science
in the Department of Electrical and Computer Engineering
University of Saskatchewan
Saskatoon

By
Michael R. W. Newton

©Michael R. W. Newton, November 2016. All rights reserved.

Permission to Use

In presenting this thesis in partial fulfillment of the requirements for a Postgraduate degree from the University of Saskatchewan, I agree that the Libraries of this University may make it freely available for inspection. I further agree that permission for copying of this thesis in any manner, in whole or in part, for scholarly purposes may be granted by the professor or professors who supervised my thesis work or, in their absence, by the Head of the Department or the Dean of the College in which my thesis work was done. It is understood that any copying or publication or use of this thesis or parts thereof for financial gain shall not be allowed without my written permission. It is also understood that due recognition shall be given to me and to the University of Saskatchewan in any scholarly use which may be made of any material in my thesis.

Requests for permission to copy or to make other use of material in this thesis in whole or part should be addressed to:

Head of the Department of Electrical & Computer Engineering
3B48 Engineering Building
57 Campus Drive
University of Saskatchewan
Saskatoon, Saskatchewan
Canada
S7N 5A9

Abstract

Single event effects have been an issue in microelectronic devices and circuits for some time, especially those used in radiation-intense environments such as space. Traditionally, devices have been tested using particle accelerator facilities for evaluation of the various single event effects phenomena. However, testing at these facilities can be prohibitive to many research groups due to costs and time availability. As a result, pulsed laser testing has evolved to become a standard, additional testing methodology for evaluating single event effects. Not only do pulsed laser facilities generally offer more flexibility in terms of cost, but it is also possible to gain additional information about the spatial and temporal nature of single event effect generation in sensitive areas of a device.

To meet the needs of the radiation effects community, pulsed laser facilities have continued to be set up around the world. One of these includes the facility at the Saskatchewan Structural Sciences Centre. An earlier iteration of the facility previously existed which utilized a different equipment set and did not have the two photon absorption capabilities that the current version does. In this thesis, a sample of the work performed at the facility using both the single and two photon absorption capabilities are provided to demonstrate its capabilities; the devices tested for single event effect response included two Hall effect sensors and a Xilinx Virtex-5 FPGA. Additionally, a description of the main features of the facility in its current form is given. Through this work, the feasibility of the facility to provide results to users, both academic and industrial, is demonstrated.

Acknowledgements

Firstly, I would like to thank my supervisor, Dr. Li Chen for his generous support and patience for the duration of this work. Without securing funding from NSERC Engage as well as providing the facility environment in which to work, this project would not have been possible and as such am grateful to Dr. Chen for this opportunity.

I also want to thank Dave Hiemstra from MDA Corporation. As a collaborator of Dr. Chen's, Dave has provided me with support in many ways. From technical help and suggestions to editing my papers, Dave's insight and outstanding knowledge in the field of radiation effects in microelectronics has been invaluable. At more times than I might want to admit, Dave's incredible patience in regards to my inability to deliver results in a timely manner has also not gone unappreciated. I think Dr. Chen is incredibly fortunate to have a collaborator such as Dave.

Out of my closest friends, I want to thank Isho Shamo for providing emotional support during the course of this work in the form of friendship and good humor. Isho always knows how to lighten the mood and has been great at helping keep up my spirits.

I also want to thank my co-supervisor and manager of the Saskatchewan Structural Sciences Centre, Dr. Ramaswami "Sammy" Sammynaiken. I have known Sammy since my final year of undergraduate work in physics, and it was he who spurned me to pursue graduate studies and put me in contact with Dr. Chen. Though often either unsaid or indirectly so, it is clear that Sammy believes greatly in my potential to perform high-caliber work, which is a great compliment coming from someone such as him.

Finally, I would like to thank my father, Darrell Newton, for helping me become the man I am today.

Contents

Permission to Use i

Abstract ii

Acknowledgements iii

Contents iv

List of Tables vii

List of Figures viii

List of Abbreviations x

1 Introduction 1
1.1 Motivation . . . 2
1.2 Objectives . . . 3
1.3 Layout of Thesis . . . 3

2 Background of Single Event Effects 5
2.1 Description of Single Event Effects . . . 5
2.2 Types of Single Event Effects . . . 8
2.2.1 Single Event Upset . . . 8
2.2.2 Single Event Transient . . . 9
2.2.3 Single Event Latchup . . . 9
2.3 Particles Used in Single Event Effect Testing . . . 10
2.3.1 Alpha Particles . . . 10
2.3.2 Protons . . . 10
2.3.3 Heavy Ions . . . 11
2.3.4 Neutrons . . . 11
2.4 Particle Accelerator Facilities . . . 12

3 Ultrafast Pulsed Lasers, Single Photon Absorption, and Two Photon Absorption: Background and Theory 13
3.1 Introduction to Lasers . . . 13
3.2 Continuous Wave and Pulsed Lasers . . . 16
3.3 Pulsed Lasers in Single Event Effects Testing . . . 18
3.4 Interaction of Light with Semiconductor Materials . . . 20
3.4.1 Single Photon Absorption . . . 22
3.4.2 Two Photon Absorption . . . 23
3.5 Testing Parameters Considered for SEE Evaluation Using a Pulsed Laser System . . . 25

3.5.1 Single Photon Absorption or Two Photon Absorption: Front Side vs. Back Side Irradiation . . . 25
3.5.2 Pulse Duration and Repetition Rate . . . 27
3.5.3 Laser Spot Size . . . 27

4 The Pulsed Laser Facility for SEE Testing at the Saskatchewan Structural Sciences Centre: Equipment and Setup 29
4.1 Background . . . 29
4.2 Facility Equipment Setup . . . 30
4.2.1 Amplification Stage . . . 31
4.2.2 Post-Amplification . . . 33
4.3 Laser Irradiation Procedures . . . 36

5 Response of Optek OMH3075 and Infineon TLE4945 Hall Effect Sensors to Single Event Effects Induced via Single Photon Absorption 39
5.1 Introduction . . . 39
5.2 Overview of Sensors . . . 40
5.3 Test Facility . . . 42
5.4 Experiment Setup . . . 42
5.5 Test Conditions . . . 44
5.6 Test Objectives . . . 45
5.7 Experimental Results: Optek Hall Effect Sensor . . . 45
5.7.1 Output Logic High and Solenoid On Test Condition . . . 47
5.7.2 Output Logic Low and Solenoid On Test Condition . . . 47
5.7.3 Output Logic High and Solenoid Off Test Condition . . . 50
5.7.4 Output Logic Low and Solenoid Off Test Condition . . . 51
5.8 Experimental Results: Infineon Hall Effect Sensor . . . 52
5.8.1 Output Logic High and Solenoid On Test Condition . . . 54
5.8.2 Output Logic Low and Solenoid On Test Condition . . . 55
5.8.3 Output Logic High and Low with the Solenoid Off Test Condition . 56
5.9 Discussion . . . 57
5.10 Conclusions . . . 58
5.11 Summary . . . 59

6 Evaluation of a Xilinx Virtex-5 FPGA Using Two Photon Absorption 60
6.1 Introduction . . . 60
6.2 Device Overview . . . 61
6.3 Experiment Setup . . . 63
6.4 Configuration Memory Results and Cross Section Correlation with Proton Data . . . 65
6.4.1 Cross Section Comparison with Proton Data . . . 69
6.5 Configurable Logic Blocks - Counters . . . 70
6.6 DSP48 - Multipliers . . . 74
6.7 Block RAM . . . 77
6.8 Damage to the Virtex-5 . . . 77
6.9 Discussion . . . 79

6.10 Summary 80

7 Summary **81**

References **83**

List of Tables

3.1 Spot size calculations for the objective lenses used at the laser facility at wavelengths of 580 nm and 1200 nm. 28

5.1 Minimum and Maximum Operating Voltage of OMH3075 and TLE4945 devices. 40
5.2 Laser Irradiation Parameters for Hall Effect Sensor Studies. 42
5.3 Test bias conditions. 45

6.1 Current and previous laser irradiation parameters for Virtex-5 FPGA studies. 64
6.2 ROI parameters for configuration memory area scan. 68
6.3 Energy threshold test for counter using continuous laser scan mode. 73
6.4 Energy Threshold of CLB Counter for Single Point Region of Interest (ROI) Laser Irradiation 74
6.5 Energy threshold test for DSP block using continuous laser scan mode. . . 76
6.6 Energy threshold of DSP for single point ROI laser irradiation. 77

List of Figures

2.1 Illustration of a single event effect. Image Credit: *COTS Journal.* 6

3.1 Light intensity output over time for a CW and pulsed laser. In this example the pulsed laser has a period of 100 μs which corresponds to a repetition rate of 10 kHz. 17
3.2 Absorption coefficient of pure silicon in cm^{-1} as a function of wavelength at room temperature [1]. 22
3.3 Charge density plot comparisons for an SPA process versus a TPA process [2]. The SPA wavelength used was 590 nm, while 1260 nm was used for TPA. 24
3.4 Illustration of front side irradiation and back side irradiation. 26

4.1 Photo of the SSSC SEE laser facility at the University of Saskatchewan. The Verdi, Vitesse, RegA, and OPA units are shown and labelled. 30
4.2 Block diagram of the SSSC SEE laser setup from a top-down view. The arrows indicate the beam paths of the lasers used. 31
4.3 Photo of the ThorLabs MPM200-SGP microscope and stage. The 50x objective lens is also visible in the picture. 35
4.4 Screen capture of the ThorImageLS software version 2.3 with a section of the Virtex-5 configuration memory being imaged by the imaging laser. The yellow box is the rectangular ROI selected. 37
4.5 Point ROI on a DUT. The yellow crosshair indicates the sole location where incoming laser pulses will be injected. 38

5.1 Block Diagram of Infineon TLE4945 HES [3]. 41
5.2 Block Diagram of Optek OMH3075 HES [4]. 41
5.3 Block diagram of the test board for the Optek and Infineon HESs. 43
5.4 Photos of the test boards for the Optek and Infineon HESs. The device under test for (b) is indicated by the black marker lines around its area. . . 44
5.5 Optek HES sensitive areas for the output logic high and solenoid on. (a) represents the areas most sensitive when the device started in the high states, while (b) represents those most sensitive when started in the low states. 46
5.6 Structures most sensitive to upset from the laser pulses. (a) is most sensitive for the high state condition, while (b) is most sensitive for the low condition. 46
5.7 Optek HES output transient pulse observed at 250 pJ for output logic high and solenoid on. 47
5.8 Optek HES output transient pulse observed at 250 pJ for output logic high and solenoid on. 48
5.9 Optek HES output voltage transient observed at 1.15 nJ for output logic low and solenoid on. 49
5.10 Optek HES output voltage transient observed at 1.75 nJ for output logic low and solenoid on. 50

5.11 HES output voltage observed at 20 pJ per pulse for the initial output logic high without the applied magnetic field from the solenoid. 51
5.12 Optek HES output voltage observed at 1.075 nJ when the output starts at a logic low state without the magnetic field applied. 52
5.13 HES structure. The red areas indicate oversaturation of the image detector pixels. 53
5.14 Infineon HES sensitive area. 54
5.15 Infineon HES Output transient pulse observed at 20 pJ for the output logic high and solenoid on. 55
5.16 HES output transient pulse at 415 pJ, for output logic low and solenoid on. 56
5.17 Infineon HES output voltage transient at 20 pJ for logic low or high with the solenoid off. 57

6.1 Genesys XC5VLX50T-FFG1136 (1C) development board. The Virtex-5 is the component in the center of the board. 62
6.2 Picture of the Virtex-5 development board under the microscope. 64
6.3 Standard and modified 6T SRAM cells. 65
6.4 Picture of an area of the Virtex-5 configuration memory. The field of view is 1440 μm $\times$ 1440 μm. The red regions indicate oversaturation of image pixels on the detector. 66
6.5 Picture of an area of the Virtex-5 configuration memory with a rectangular ROI. 67
6.6 Errors experienced by the Virtex-5 configuration memory as a function of laser pulse energy. 69
6.7 Cross section per bit as a function of laser pulse energy of the configuration memory. 70
6.8 The 3 456-bit counter columns as viewed under the microscope. On the left is a BRAM column, while the right side is an input-output block. . . . 71
6.9 81 x 81 μm^2 view of a single counter column used for pulsed laser testing. . 72
6.10 DSP48 column located in the center between some configuration memory columns. 75
6.11 DSP48 column located in the center between some configuration memory columns. 76
6.12 Location of permanent damage caused by the laser. The affected area is circled in blue. 78

List of Abbreviations

BBO	Beta Barium Borate
BRAM	Block Random Access Memory
CLB	Configurable Logic Block
COTS	Commercial Off-The-Shelf
CW	Continuous Wave
DUT	Device Under Test
DRAM	Dynamic Random Access Memory
EADS	European Aeronautic and Defense Space Company
EDAC	Error Detection and Correction
EM	Electromagnetic
ESA	European Space Agency
FPGA	Field Programmable Gate Array
FWHM	Full Width at Half Maximum
HeNe	Helium-Neon
HES	Hall Effect Sensor
IC	Integrated Circuit
ITRS	International Technology Roadmap for Semiconductors
JPL	Jet Propulsion Laboratory
LET	Linear Energy Transfer
MBU	Multiple-Bit Upset
NRL	Naval Research Laboratory
ROI	Region of Interest
RTL	Register Transfer Level
SEB	Single Event Burnout
SEE	Single Event Effect
SEGR	Single Event Gate Rupture
SEL	Single Event Latchup
SET	Single Event Transient
SEU	Single Event Upset
SPA	Single Photon Absorption
SRAM	Static Random Access Memory
SSSC	Saskatchewan Structural Sciences Centre
TID	Total Ionizing Dose
TPA	Two Photon Absorption

Chapter 1

Introduction

In his 1965 paper *Cramming more components onto integrated circuits*, Gordon Moore predicted that the number of components that could fit into a microelectronic device or integrated circuit (IC) would double every year [5]. Ten years later, Moore revised the time scale to every two years. This prediction of exponential growth came to be known as Moore's law. While not an actual physical or natural law, Moore's law has been observed to largely hold true over the past forty years. The advancements resulting from this trend have ushered in a digital revolution leading to widespread use of numerous electronic devices in all areas of society. Moore's law has been of particular interest to the semiconductor industry as it has provided an outline for the evolution of the feature size of the transistor. In 1971, the semiconductor process achieved was 10 μm. Today it is 14 nm, according to the International Technology Roadmap for Semiconductors (ITRS). In terms of transistor count, ICs created in the early 1970s contained several thousand transistors; those developed today have several billion. While the rate of scaling has continued relatively unabated, it is believed that Moore's law has begun to slow and will continue to decelerate as the next feature sizes are realized.

Moore's law has led to many advancements in IC design by reducing power consumption, area, and cost while simultaneously increasing computational ability. However, with this downscaling in feature size the devices used in radiation-intensive environments such as space have exhibited an increased susceptibility to a phenomenon known as single event effects (SEEs).

A single event effect, or SEE, is fundamentally the result of an energetic, often ionized particle interacting with a sensitive node of an electronic device. As the particle passes through the device it will collide with atoms in the substrate, ionizing the material and

generating a track of electron-hole pairs. If the excess charge is collected around the depletion region of a p-n junction it can cause current and voltage variations, affecting the behavior of the device. SEEs can cause a wide variety of effects, ranging from small glitches in device output to complete failure of a whole system.

1.1 Motivation

Coupled with its random nature and the presence of a wide spectrum of energetic particles in high-altitude and space environments, it is clear that SEEs pose a significant threat to the normal, reliable operation of sensitive electronics in these areas.

The study of SEEs has been especially motivated by events observed on large-scale projects such as the Voyager and Pioneer space probes as well as the Hubble space telescope. Since the early 1970s, there have been approximately 4,500 known incidents in space systems due to radiation effects [6]. As more data and research continue to be produced, designers and manufacturers in the field of radiation-hardened electronics seek to mitigate the effects of SEEs on their devices. To do so, models are constructed that calculate the characteristics of the device, such as its electrical properties and charge collection. Additionally, the radiation environment the device will be exposed to must also be modelled and analyzed to predict the rates at which SEEs will occur. However, it is not always possible to extract sufficient data to predict device behavior from modelling alone. Therefore, testing in a laboratory setting is essential to the evaluation of the SEE response of a device. The data obtained from these tests often form the basis for the error rate prediction of a given device.

Conventional testing of SEEs has often been performed at particle accelerator facilities that supply a range of particle types with various energies. This allows users to expose their devices to similar radiation conditions as those found in ground and space environments. However, these facilities have often been difficult to access due to factors such as cost and availability. As a result, pulsed laser sources have been developed as an additional method to test for SEEs. They provide several advantages over accelerator facilities, which will be discussed further in other chapters. As pulsed laser sources have matured as an SEE evaluation tool it has motivated research groups to create and develop

their own facilities to allow for this type of testing.

1.2 Objectives

The primary objectives of this thesis are as follows:

- To describe the development and standard operating procedures of the SEE pulsed laser facility at the Saskatchewan Structural Sciences Centre (SSSC) located at the University of Saskatchewan (U of S).
- To demonstrate the utility and capabilities of the U of S pulsed laser facility to evaluate the SEE response of microelectronics and ICs. This is done through a selection of devices researched using the pulsed laser single and two photon absorption techniques that the facility equipment is capable of providing.

1.3 Layout of Thesis

The remainder of this thesis is organized as follows. In Chapter 2 the background information relevant to SEEs is presented and discussed. It starts by explaining what SEEs are, then follows by describing some common types and the particles that cause them. The chapter concludes with an overview of some of the accelerator facilities available for SEE testing.

Chapter 3 presents the theory and information necessary to understand pulsed lasers in the context of SEE testing. The chapter begins with a general introduction to lasers, then compares the continuous wave and pulsed laser types. Ultrafast pulsed lasers are also described in this discussion. The main advantages that pulsed lasers have over particle accelerators are also described. Next, the interaction of light with semiconductors and the single and two photon absorption processes are presented. Both absorption processes have advantages and disadvantages for SEE evaluation. The remainder of the chapter is dedicated to discussing the testing parameters that must be taken into account when performing pulsed laser testing on sensitive devices.

The setup, equipment, and features of the SSSC pulsed laser facility for SEE testing are presented in Chapter 4. As the facility and setup was quite new and previously had not had any other full time users before this thesis, considerable work was performed in learning how all the individual components interact and integrate with each other and form the overall larger system. The results of this undertaking enabled a standard operating procedure to be developed for users of the facility as well as ensuring that system performance will remain consistent on a day-to-day basis.

Chapter 5 presents the results of testing two different models of Hall Effect sensors using the single photon absorption capabilities of the facility. Chapter 6 presents the results of testing a Xilinx Virtex-5 FPGA using the facility's two photon absorption capabilities. Previous testing of the FPGA was performed at the laser facility, and the work presented here is a continuation and confirmation of that work. Both of these chapters represent the first devices tested using the SSSC pulsed laser facility.

A brief summary as well as some recommendations for future work at the SSSC laser facility are given at the end of this thesis.

Chapter 2

Background of Single Event Effects

In this chapter, the background information necessary to understand the single event effects phenomena is provided. To accomplish this, a description of the interaction mechanisms of SEEs along with a brief overview of their history is given. Additionally, several notable types of SEEs are explained. The types of radioactive particles that cause SEEs, as well as their use at accelerator facilities are also described.

2.1 Description of Single Event Effects

The concept of SEEs was first predicted in a paper from 1962 by J.T. Wallmark and S.M. Marcus [7]. In 1975, thirteen years later, Binder et al. reported anomalies in satellites that were considered the first occurrences of single event upsets (SEUs) [8]. Unfortunately, these papers were mostly ignored when published as SEEs were not considered a significant threat to electronic systems at the time. However, more occurrences of SEEs started to be observed. One of the first investigations that motivated further study of SEEs was performed by May and Woods in 1979 [9]. In fact, their observances did not come from space but rather in a dynamic random access memory (DRAM) on the ground. It was found that the packaging materials contained trace amounts of thorium and uranium which emitted alpha particles and caused SEUs in the ICs. Since then, more problems caused by SEEs continued to be reported. The study of SEEs for space, avionics, and military systems is essential to ensuring mission success.

As briefly mentioned in Chapter 1, an SEE is the result of an energetic particle penetrating into the sensitive nodes of a device, ionizing the material and generating a track of electron-hole pairs. Often, the material is silicon due to its ubiquity in the IC industry.

As the name suggests, SEEs are named as such because they are the result of a single particle acting on a device. This is in contrast to other radiation effects such as total ionizing dose (TID) that describe the cumulative, longer term results of energy deposited within a device by a large number of particles. TID is also of interest to the radiation effects community as accumulated dose will degrade device performance and in sufficiently high amounts can eventually cause components to cease normal operation entirely. Unlike TID and other total dose radiation, which have global effects over the entire device, a single event is localized to a specific area where the particle hits.

When an energetic particle enters a semiconductor it loses energy through Rutherford scattering, which is a result of the Coulomb interaction. As the particle slows due to the energy loss through interaction with the nuclei of the semiconductor lattice it generates an ionization trail in its wake that produces unbound electron-hole (e-h) pairs. Since these e-h pairs did not exist before the particle struck the device they act as excess mobile charge carriers. Subsequently, this can lead to additional charge deposition in sensitive nodes, causing unwanted changes in the voltage and current properties of the device. Figure 2.1 illustrates this process.

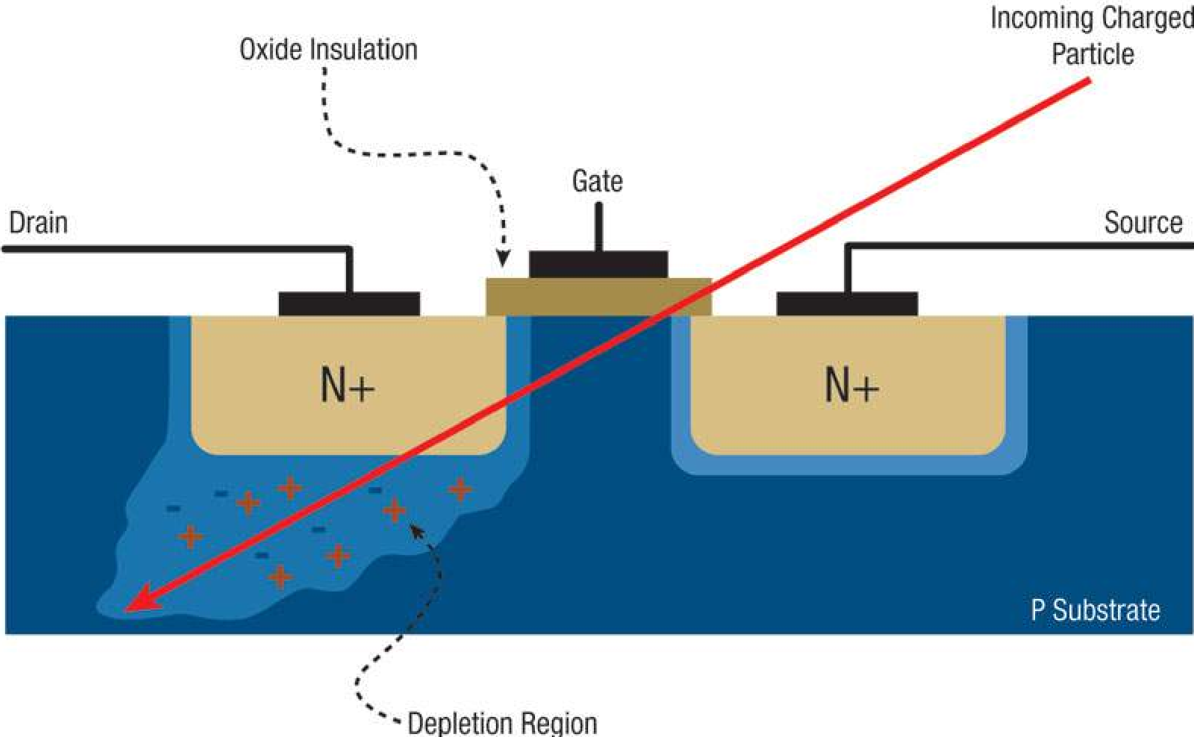

Figure 2.1: Illustration of a single event effect. Image Credit: *COTS Journal.*

As can be seen in Figure 2.1, the potential of the depletion region is distorted by the particle into a funnel shape. This is known as the field-funneling effect. The deposited minority charge carriers are collected promptly, resulting in a large increase in charge accumulation. After the funnel region recovers from the distortion, the majority charge carriers will slowly diffuse into the depletion region.

There are four primary types of particles involved in SEEs and SEE testing: alpha particles, heavy ions, protons, and neutrons. Depending on the type, they can generate SEEs through both direct and indirect ionization. For the case of direct ionization, a particle such as a heavy ion enters the device, deposits a track of ions along its trajectory path, and then exits the device. Figure 2.1 is an example of direct ionization. In contrast, indirect ionization occurs when a particle such as a proton undergoes a nuclear reaction with the semiconductor material, producing a heavy ion that will deposit sufficient energy to cause an SEE. The short range recoil of the collision produces the ionization path.

As the particle passes through a device, it loses energy to the electrons in the material. The nuclear physics community describes this as the average energy loss per unit length, or stopping power. While quite similar, the radiation effects community prefers to use linear energy transfer (LET) to describe particle energy loss, and is given by

$$LET = -\frac{1}{\rho}\frac{dE}{dx} \tag{2.1}$$

where ρ is the density of the material. The units of LET are often given in MeV$\cdot$cm^2/mg. LET has the advantage that it includes the material density term so that the energy measured becomes independent of the material type.

Fundamental to the study of SEEs is the cross section concept. Similar to LET, it has its origins in nuclear physics. The problem is essentially the measurement of what happens when one group of particles is incident on another group of particles. Since the area of the nuclei of both the incident and receiving particles are very small relative to the spacing between them, there is a small probability of an incident particle hitting a nucleus in its path. Therefore, the cross-sectional area measures the probability of a target particle being hit and in general is given by

$$\sigma = \frac{N}{\Theta} \tag{2.2}$$

where N is the number of SEEs observed and Θ is the fluence of the incident particles, often given in particles/cm^2. While there are some variations in how cross section can be calculated depending on the system they all derive from this base assumption. For example, sometimes it is desired to calculate the per-bit cross section which takes the obtained value for the cross section and divides it by the number of memory elements exposed to a radiation source.

2.2 Types of Single Event Effects

Single event effect is actually an umbrella term used to describe various types and subtypes of effects. Additionally, these SEE types can also be classified as soft or hard errors. Soft errors are those that disrupt the normal operation of a device or circuit but can be corrected by using external stimuli such as a system reset, device reconfiguration, or power cycle. Some types of soft error SEEs include single event upset (SEU), single event transient (SET), and single event latchup (SEL). Hard errors, also known as permanent errors, are the types of SEEs that cause physical damage to a system that cannot be corrected. Examples of these SEE types include single event induced burnout (SEB) and single event gate rupture (SEGR). Both hard and soft errors are important in the study of SEEs. This work is more focused on the study of soft errors, and as such the SEU, SET, and SEL types will briefly be discussed here.

2.2.1 Single Event Upset

A single event upset (SEU) is the result of an incoming particle changing the initial state of a circuit component, such as a latch or bit in a static random access memory (SRAM). Essentially, an SEU overwrites previous information in the device. As previously mentioned, some of the first SEUs observed were from alpha particles in the packaging materials of DRAMs.

There are many methods of correcting for SEUs, such as adding redundancy and opti-

mizing of current designs. Numerous types of error detection and correction (EDAC) also exist. Still, SEUs can be problematic if especially critical nodes are hit, such as a configuration memory bit in a field-programmable gate array (FPGA). Additionally, multiple-bit upsets (MBUs) are also possible. Caused by a single particle upsetting multiple bits simultaneously, MBUs are especially detrimental as they can defeat several methods of SEU mitigation.

2.2.2 Single Event Transient

Single event transient (SET) refers to the generation of an erroneous signal pulse due to an incoming particle. They can occur in both analog and digital circuits. Asynchronous in nature, SETs are problematic as they can propagate through circuit paths and reach components such as latches or flip-flops. If they pass as legitimate signals then the system operation can be compromised. If one is lucky, the timing of an SET will be such that it is overwhelmed by the real synchronous signals of the system. However, for example, if its pulse duration is on the order of the setup and hold times of a sequential logic component then it is much more likely an SET will be processed. Newer systems are also increasingly susceptible to SETs as their clock rates increase.

The amplitude and duration of an SET pulse are important in characterizing the device response as they indicate the charge collection of the component that experienced the particle strike.

2.2.3 Single Event Latchup

Single event latchup (SEL) is the condition that results from an incoming particle inducing a device into a high current state, effectively shorting the circuit and causing the device to lose functionality. If not corrected for by a power cycle or other means, SEL can introduce many unwanted effects into a device. Generally, if a latchup condition is not removed relatively quickly a system can fail completely. This is often due to melting from excessive heat caused by the induced current flow. Therefore, SELs can be classified as both hard and soft errors.

2.3 Particles Used in Single Event Effect Testing

Designers and engineers in the radiation effects community utilize accelerator facilities around the world that provide particle beams relevant to their SEE evaluations. There are four primary types of particles responsible for SEEs in sensitive systems. They include alpha particles, protons, neutrons, and heavy ions. This section will briefly describe each of these.

2.3.1 Alpha Particles

An alpha particle is a helium nucleus, consisting of two protons and two neutrons. Due to its relatively large mass and strong interaction with matter, the range of alpha particles in a medium can be quite small, from less than a tenth of a millimeter in silicon or tissue to only a few centimeters in air [10]. Therefore, most of the dangers posed by alpha particles do not come from external sources but rather from impurities present in the IC packaging material. As mentioned earlier, some of the first observed SEEs were caused by alpha particles from packaging material impurities. Trace amounts of uranium and thorium isotopes in the packaging are the most common alpha particle sources. As they are embedded in the material itself they may be sufficiently close to sensitive nodes that an alpha particle can reach. Fortunately, IC manufacturing processes have improved in removing impurities from the final device, reducing the risk of an upset occurring from an alpha particle. At the same time, dedicated alpha particle sources can be useful for studying SEEs. Americium-241, which is also found in household smoke detectors, is one example.

2.3.2 Protons

A proton is a subatomic particle with a positive elementary charge $+q$. The number of protons within an atomic nucleus defines the element type of that atom. A single proton on its own is a positively charged hydrogen atom. Due to their ubiquity in space environments protons are of high interest to SEE studies. In the proton belts around Earth there is a flux between 10^7 and 10^9 protons/cm^2 per day with energies greater

than 30 MeV, which is approximately the minimum energy a proton needs to penetrate a spacecraft and cause upsets in components [11].

Protons are capable of causing upset through both direct and indirect ionization. If a proton exceeds the energy threshold of a device it will directly ionize the medium and generate an upset. As well, if its energy is sufficiently high a proton will collide with an atom in the material and cause a nuclear reaction. The action of the recoil from the generated heavy ion causes the SEE. Approximately 1 in every 10^5 protons will undergo a nuclear reaction in a silicon device [7].

2.3.3 Heavy Ions

Heavy ions are defined as any atomic nucleus with a mass greater than an alpha particle and a net electric charge. Effectively, this means any nucleus with an atomic number greater than 2 can be considered a heavy ion. As many of them originate from outside the solar system, they can also be considered a galactic cosmic ray. They are found everywhere in interplanetary space, though protons compose the majority of particles in many space environments.

Heavy ions cause SEEs via direct ionization in the materials they pass through. They are highly energetic with particle energies on the order of several GeV and up. This makes them extremely difficult if not impossible to stop with any practical amount of shielding. The background heavy ion flux in space is approximately 1-10 particles/cm^2 per second [2]. It is clear that heavy ions pose a threat to the reliability of space electronics.

2.3.4 Neutrons

Neutrons are an electrically neutral subatomic particle. Due to this, they are quite difficult to stop. As they do not experience attraction or repulsion to ionized particles, neutrons indirectly ionize materials through collisions with nuclei. In fact, some of the most effective shielding comes from materials with low atomic numbers, especially those that contain hydrogen [2].

Neutron-induced upsets are notably problematic in avionics systems used in high altitude atmospheric environments. As well, SEEs due to neutrons at the ground level have

also been observed and reported.

2.4 Particle Accelerator Facilities

Ideally, the SEE response of a device could be measured simply by placing it in a space environment. However, this is often unfeasible for many reasons. Instead, particle accelerator facilities around the world that supply protons and heavy ions are often used, and some of the most well known are listed here. Both total dose and SEE testing can be accomplished at these facilities. While accelerators serve a wide variety of academic and industrial interests, some of the most notable proton facilities used for SEE testing include the Crocker Nuclear Laboratory at the University of California Davis campus, Michigan State University Cyclotron Laboratory, and until recently (December 2014) the Indiana University Cyclotron Facility. As a source of Canadian pride, TRIUMF at the University of British Columbia in Vancouver houses a world-class proton irradiation facility utilized by the radiation effects community as well as many other research groups.

Heavy ion facilities used most commonly for SEE testing include Brookhaven National Laboratory, Texas A & M, Lawrence Berkeley Labs, Michigan State University's National Superconducting Cyclotron Laboratory, and the Heavy Ion Facility at UCL in Belgium. Many of these facilities are capable of offering either single ion beams or ”cocktail” beams consisting of several ion types to cover a broader LET range and partially simulate a space environment. Unfortunately Canada does not currently have any heavy ion facilities capable of serving the radiation effects community. Due to most facilities being located in the United States, most heavy ion SEE testing is performed there.

Chapter 3

Ultrafast Pulsed Lasers, Single Photon Absorption, and Two Photon Absorption: Background and Theory

This chapter aims to outline the background and theory of pulsed lasers as they relate to SEE evaluation. To do so, firstly a brief general introduction to lasers is given. Next, the concepts and principles necessary for pulsed laser operations are described, followed by their applications to SEE testing in microelectronic devices. Afterwards, the description of the single and two photon absorption phenomena in the context of SEE evaluation is provided. Finally, the testing parameters that must be taken into consideration when using a pulsed laser are presented.

3.1 Introduction to Lasers

Firstly, what is a laser? The name itself is actually an acronym for "Light Amplification by Stimulated Emission of Radiation." Based on the initial work by Charles Townes and Arthur Schawlow, the first laser was constructed in 1960 by Theodore Maiman. Around the time of its invention, the laser was referred to as, "A solution in search of a problem [12]." Since then, lasers have certainly been used to solve many problems. Today, lasers are ubiquitous; from high end research labs to medical tools and consumer electronics, lasers continue to find use in a very diverse range of fields.

In general, a laser is any device that emits light due to an optical amplification process via stimulated emission of electromagnetic radiation. This criterion separates lasers from other light sources. In addition, lasers are defined by their ability to emit spatially and

temporally coherent light. The meaning of stimulated emission and coherence will be explained here.

From quantum mechanics comes the famous Planck-Einstein formula that shows the relation between the energy and wavelength of a photon and is given by

$$E = h\nu = \frac{hc}{\lambda} \tag{3.1}$$

where h is Planck's constant, c is the speed of light, and ν/λ are the frequency/wavelength of the photon, respectively. As well, from quantum mechanics it is also known that electrons in an atom occupy discrete energy levels. The electronic structures of different atoms can vary considerably and can be quite complex. If an electron occupies an energy level E_1 it can be excited into a higher energy state E_2 through absorption of a photon with energy equivalent to the difference between the two states. That is, if $h\nu = E_2 - E_1$ then the electron will be induced into the state with E_2 [13]. This change in the electron configuration of the atom induces it into an excited state. In a symmetrical process, when the electron transitions back down to E_1 it will emit a photon with energy $h\nu$. The downward transition can occur spontaneously or can be stimulated to do so.

In spontaneous emission the electron falls down to E_1 from E_2 provided the state E_1 is unoccupied by another electron, and then emits a photon in a random direction. Stimulated emission, by contrast, involves an incoming photon with energy $h\nu = E_2 - E_1$ inducing the electron in E_2 to transition down to E_1. In this situation, the emitted photon has the same properties as the incoming photon, including energy, direction, phase, and polarization. This is a fundamental principle in laser physics as it forms the basis for optical amplification. To obtain an overall net positive amplification, the incident photons should not be absorbed by the electrons at E_1. Rather, the majority of the electrons must be at E_1. When this happens the result is a population inversion. However, under normal equilibrium conditions, due to Boltzmann statistics a system with only two energy states will never be able to produce a population inversion as the incoming photons will produce as many upward transitions as downward stimulated emissions [13]. Therefore, in general there must be 3 or more electronic states to sustain a laser system. It is noted that the energy structures of different lasers can be considerably complex and generally include

more than 3 states when all accounted for.

To build a laser, three main components are required: a pump source, gain medium, and optical resonator/cavity, which are listed here [14].

- A *pump source* supplies the energy required to excite the atoms in the gain medium to the necessary energy level(s). Methods of optically pumping a medium include using an intense lamp, gas discharge, the current in a semiconductor or semiconductor heterostructure, and even another laser, among others.

- The *gain medium* is the material in which the optical amplification via stimulated emission takes place. Often it is located inside the resonator and can either partially or completely occupy the space contained within. The medium can be composed of many different material types in all states of matter.

- An *optical resonator*, or cavity, is required in order to output the lasing emission. The resonator also has the task of storing the coherent electromagnetic (EM) field and enabling its interaction with the gain medium. Fundamentally, a resonator consists of two mirrors with reflectances R_1 and R_2. R_1 has a reflectance close to 1 (almost all of the light is reflected by this mirror) while R_2 generally has a smaller value to serve as an output coupler so that the laser beam can be transmitted out of the resonator. The EM wave oscillations within the resonator build up in power with each pass between the mirrors at a rate faster than the losses accumulated due to transmission and diffraction.

With these three components many different types of lasers and laser systems have been designed. With advances in numerous scientific fields many different gain media have been utilized to produce stimulated lasing emissions. The original laser used a ruby crystal as the gain medium. Shortly after, the now famous helium-neon (HeNe) laser was invented, which used a mixture of helium and neon gases. As technologies in the semiconductor industry advanced, diode-based lasers became feasible, a trend which continues today.

What separates a laser from a light bulb? Coherence. In a laser system, the output resulting from stimulated emission provides the conditions necessary for the output beam

to be coherent both spatially and temporally. The white light spectrum of a light bulb is inherently incoherent. If the phase of any part of an EM wave can be predicted from any other part of the wave, the radiation is said to be perfectly coherent in the spatial and time domains. A classic example of perfect coherence is a pure sine wave. Of course, in any practical system a real wave can only exist over a given length and time, which for a laser are referred to as the coherence length and coherence time, respectively. As might be expected, the coherence length and time of a laser beam can vary considerably based on the design.

3.2 Continuous Wave and Pulsed Lasers

Lasers can be characterized by the period of time over which they emit power. In this classification there are two main types: continuous wave (CW) and pulsed. A CW laser outputs a stable average beam power and therefore its intensity does not vary by an appreciable amount over time. Pulsed lasers, on the other hand, emit their energy in a train of discrete, repetitive, periodic pulses. That is, they essentially cycle their lasing emission on and off with some frequency. In laser physics this frequency is often referred to as the repetition rate and is measured in Hz. Again, depending on the design, a pulsed laser can have a repetition rate less than 1 Hz or greater than 100 GHz [15]. Additionally, each pulse in the train exists over a certain period of time. The literature variously refers to this value as the pulse duration, length, or width. Figure 3.1 illustrates the difference between CW and pulsed lasers.

One of the most important methods of checking laser performance is by measuring the power or energy output. A CW laser is fairly straightforward. However, for a pulsed laser, it is important to discern the difference between its peak and average power output. The amount of energy contained within each pulse also becomes an important factor. The peak power of a pulsed laser is given by [16]

$$P_{peak} = \frac{E_{pulse}}{t} \tag{3.2}$$

where E_{pulse} is the energy per pulse and t is the pulse duration. In contrast, a pulsed

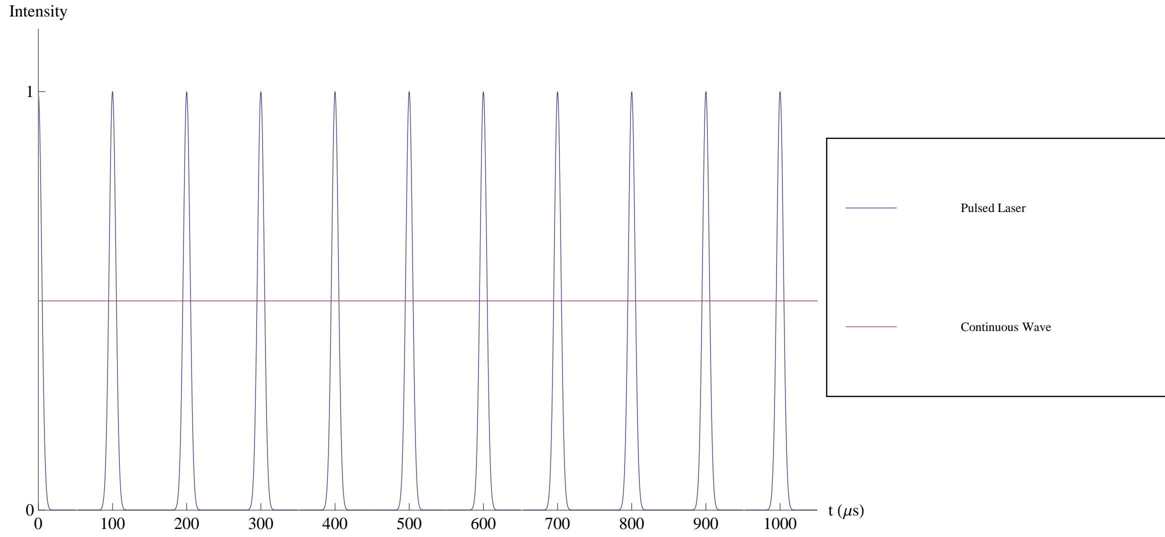

Figure 3.1: Light intensity output over time for a CW and pulsed laser. In this example the pulsed laser has a period of 100 μs which corresponds to a repetition rate of 10 kHz.

laser's average power is described by

$$P_{avg} = E_{pulse} \cdot f \tag{3.3}$$

where f is the repetition rate. Depending on the experimental requirements both the peak and average power may be important to consider. In the field of SEE laser testing the average energy per pulse is often used as the average power can be easily measured using a power meter.

The pulse durations for laser systems can range over a considerable scale. Some laser systems have pulse durations as long as several milliseconds (10^{-3}) while in others the duration can be as short as a few femtoseconds (10^{-15}). Pulsed lasers with pulse durations lower than 100 picoseconds belong to a class known as ultrafast lasers, also known as ultrashort pulse lasers [17]. Sub-picosecond lasers may also be referred to as femtosecond lasers. Often, these lasers make use of mode-locking to achieve their characteristic short, intense pulses. Due to their very short pulse duration, ultrafast lasers can have extremely high peak powers. For example, an ultrafast laser with a pulse energy of 100 nJ and pulse duration of 100 fs would have a peak power of 1 MW. The peak power of almost all ultrafast lasers is higher than the power provided by CW lasers which mostly top out in

the kW range.

It should be noted that there are no other devices aside from femtosecond lasers that are capable of producing events (pulses) on such a short time scale. For example, pulses in the femtosecond range occur faster than the formation and dissociation of many chemical bonds in molecular structures. As a result of the short pulse duration and high peak power, femtosecond lasers have enabled a considerable body of research to be undertaken in fields as diverse as femtochemistry and nonlinear microscopy. More specifically, much of this work has been possible due to the nonlinear effects resulting from the properties inherent in femtosecond lasers. One of these effects is the two photon absorption process which is utilized to test for SEEs in microelectronics in the present day.

3.3 Pulsed Lasers in Single Event Effects Testing

For the past approximately 30 years, pulsed laser testing has been used by a number of research groups primarily around the United States and Europe, with much of the early motivation being to supplement the testing being performed at particle accelerator facilities. The theoretical background of pulsed laser testing of SEEs actually dates back to 1965, where Habing proposed that light from an unfocused pulsed laser source could be used to simulate dose rate effects caused by electrons and gamma rays since both photons and particles are capable of ionizing atoms by liberating electrons from them [18]. However, it was not until 1987 that the first use of focused pulsed lasers to specifically evaluate SEEs was reported [19]. Since then, research groups have continued to report the value of using pulsed lasers to investigate SEEs in various devices.

Pulsed laser sources have been increasingly used as a tool to study SEEs in sensitive devices. There are several reasons for this advancement. Firstly, they offer experimental advantages over accelerator-based testing. Pulsed laser irradiation provides spatial and temporal information that assist in analyzing when and where a device experiences SEEs. Additionally, compared to energetic particles, x-ray, and gamma ray sources, pulsed lasers do not cause potential cumulative damage due to dose effects. Another significant factor is the cost. Generally, use of accelerator facilities can be considerably expensive, often costing upwards of several thousand dollars per hour. Clearly, this can be prohibitive,

especially for smaller groups and companies that want to test their devices but may not have the financial backing. Availability of accelerator facilities can also be fairly limited. Therefore, pulsed lasers offer a few practical advantages over accelerators in addition to the parametric advantages.

The mechanisms by which laser pulses and particles generate electron-hole pairs in sensitive devices differ, thus resulting in different charge track profiles. Laser pulses are composed of photons which are absorbed by the material to generate electron-hole pairs, whereas particles primarily do so via the Coulomb interaction. For a Gaussian beam of laser light the charge track profile decreases exponentially as a function of distance within the material, but with heavy ions it increases gradually and reaches a maximum at the Bragg peak before rapidly decreasing to zero. The differences in charge track profiles have raised questions about whether pulsed lasers can accurately model and generate the SEEs induced by ions in a radiation environment. However, the literature published over time has consistently demonstrated the viability and applicability of pulsed lasers to investigating SEEs [20]. A wide variety of devices in a wide variety of processes have been studied. Some examples include bipolar circuits, CMOS technologies, memory cells, and power devices. Thanks to considerable work done in this field, pulsed laser systems have overcome many challenges to mature into the testing method widely accepted by the radiation effects community today.

Broadly speaking, charge generation in materials via particles depends on the energy and atomic number, while the charge generated by laser pulses depend on optical parameters such as wavelength, optical components used, photon density, and absorption process. Each of these factors must be considered when evaluating SEE response and will be discussed further in the chapter. Specifically, the single and two photon absorption processes as they relate to SEE generation in semiconductor materials are of interest.

3.4 Interaction of Light with Semiconductor Materials

In semiconductor materials, the propagation and absorption of light are described by the following differential equations in terms of the irradiance, phase, and charge carrier density, respectively [21][22]:

$$\frac{dI(r,z,t)}{dz} = -\alpha(\lambda)I(r,z,t) - \beta_2(\lambda)I(r,z,t)^2 - \sigma_{ex}N \cdot I(r,z,t) \tag{3.4}$$

$$\frac{d\Phi(r,z,t)}{dz} = \beta_1 I(r,z,t) - \gamma_1 N(r,z,t) \tag{3.5}$$

$$\frac{dN(r,z,t)}{dt} = \frac{\alpha(\lambda)I(r,z,t)}{h\nu} + \frac{\beta_2 I(r,z,t)^2}{2h\nu} \tag{3.6}$$

where r and z are the radial and longitudinal positions, σ_{ex} is the absorption cross-section for photons by free electrons, γ_1 is the refraction coefficient due to free carriers, α is the linear single photon absorption coefficient, and β_1 and β_2 are the two photon absorption coefficients that arise from the real and imaginary parts of the third order nonlinear optical susceptibility, respectively [23]. As will be seen, these equations (especially 3.4) will be modified depending on if either the single or two photon absorption process is exclusively used.

The two photon absorption coefficient β_2 is given by [22]:

$$\beta_2 = \frac{K\sqrt{E_p} f(2h\nu/E_g)}{n^2 E_g^3} \tag{3.7}$$

where K is a material independent constant, n is the linear refractive index, and E_g is the band gap energy. The form of the function f depends on the assumed electronic band structure. Finally, $E_p = 2P^2 m_e/\hbar^2$, where P is the Kane momentum and m_e is the electron mass.

Equation 3.4 describes the change in irradiance of the incoming light as a function of propagation distance into the material. Note that the terms higher than second order have been omitted. The third term can indirectly affect a pulsed laser experiment by

contributing to changes in the linear and nonlinear absorption properties, thus altering the pulse propagation and charge carrier generation within the medium.

Semiconductor materials are characterized by their band gap, which is essentially the minimum energy required to excite an electron in a bound state in the valence band to an unbound state in the conduction band. While the following discussion can be generally applied to many semiconductors it will be focused towards silicon due to its ubiquity in electronic manufacturing industries. It is well known that pure silicon has an indirect band gap of $\sim$1.11-1.12 eV at room temperature. Its absorption of light as a function of wavelength is also well characterized, the spectrum of which is shown in Figure 3.2 [1]. With knowledge of these two properties combined with the propagation equations it is possible to predict if light incident on a silicon surface will be absorbed by single or two photon absorption.

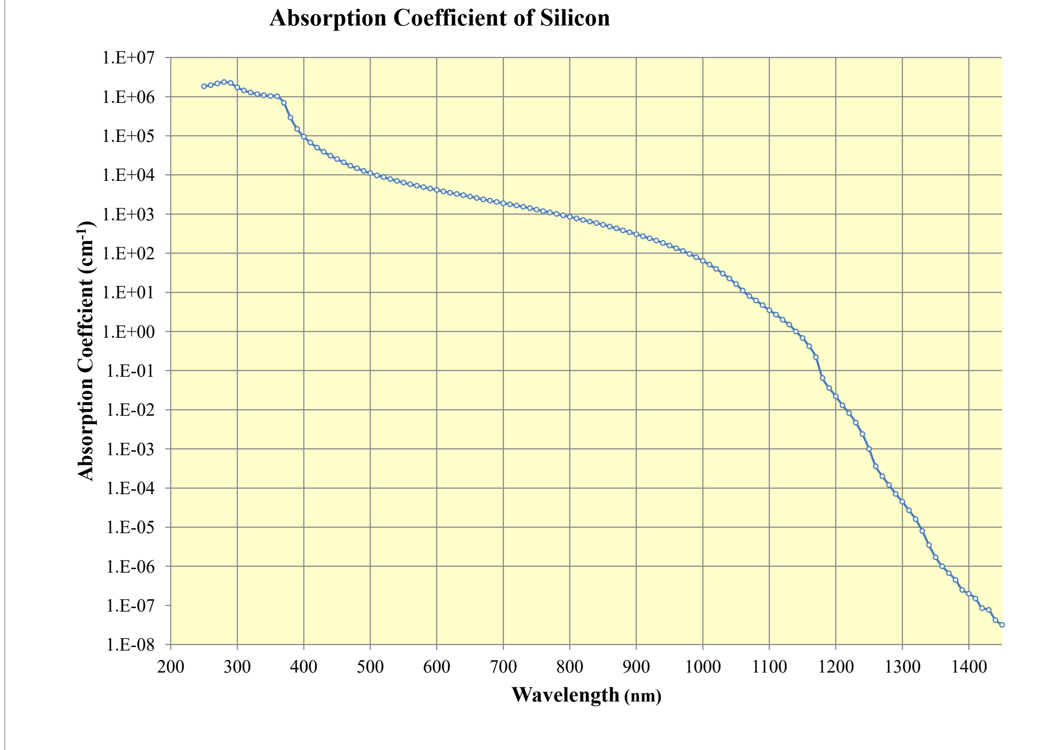

Figure 3.2: Absorption coefficient of pure silicon in cm^{-1} as a function of wavelength at room temperature [1].

3.4.1 Single Photon Absorption

Photons with energies exceeding the band gap of the semiconductor will be directly absorbed to generate electron-hole pairs. This is known as single photon absorption (SPA), or linear absorption. Equation 3.1 dictates the energy a photon will have as a function of its wavelength. In silicon, the band gap is 1.11 eV which conveniently corresponds to a photon with a wavelength of 1,100 nm. Therefore, to ensure nonlinear absorption effects are negligible, a pulsed laser wavelength should be selected that is below approximately 1,100 nm. The wavelength range for SPA is generally considered to encompass the visible and near-infrared up to 1,100 nm.

When the irradiance (often given as $\mathrm{W/cm}^2$) is sufficiently small and the nonlinear

effects can be neglected, the solution to Equation 3.4 becomes

$$I(z) = I_0 exp(-\alpha(\lambda)z) \tag{3.8}$$

where I_0 is the irradiance at the surface of the material and z is the depth below the surface. This is a form of Beer's Law which is well known and is the overwhelmingly dominant absorption process for SPA. As the irradiance is a maximum at the surface the density of charge generated is a maximum there as well.

3.4.2 Two Photon Absorption

For a photon with a wavelength longer than 1,100 nm, and thus insufficient energy to overcome the band gap of silicon, the terms in Equation 3.4 describing the linear and free carrier absorption can be neglected, whereas for SPA the nonlinear component was neglected. In this case, the solution for Equation 3.4 becomes

$$I(z) = \frac{I_0}{1 + \beta_2 I_0 z} \tag{3.9}$$

When the irradiance I_0 is sufficiently low, light will pass through the silicon relatively unabated. However, if I_0 is sufficiently high then the term in the denominator will become non-negligible and the light will be attenuated and absorbed by the silicon by a process known as two photon absorption (TPA). Conceptually, the TPA process is fairly simple to understand. After the conditions enabling TPA are met, two photons that are spatially and temporally close will be simultaneously absorbed by the silicon and generate one electron-hole pair. In another way of thinking, the silicon acts as if it "sees" one photon with twice the energy, or half the wavelength of the incoming two sub-band gap photons. While TPA has been utilized in other confocal multi-photon microscopy fields, its application to SEE testing in sensitive devices was first demonstrated to be feasible approximately 15 years ago at the U.S. Naval Research Laboratory [2]. Since then, several pulsed laser facilities around the world have been configured to test for SEEs using TPA, including the lab at the Saskatchewan Structural Sciences Centre (SSSC).

For efficient charge generation via TPA, several important conditions need to be met.

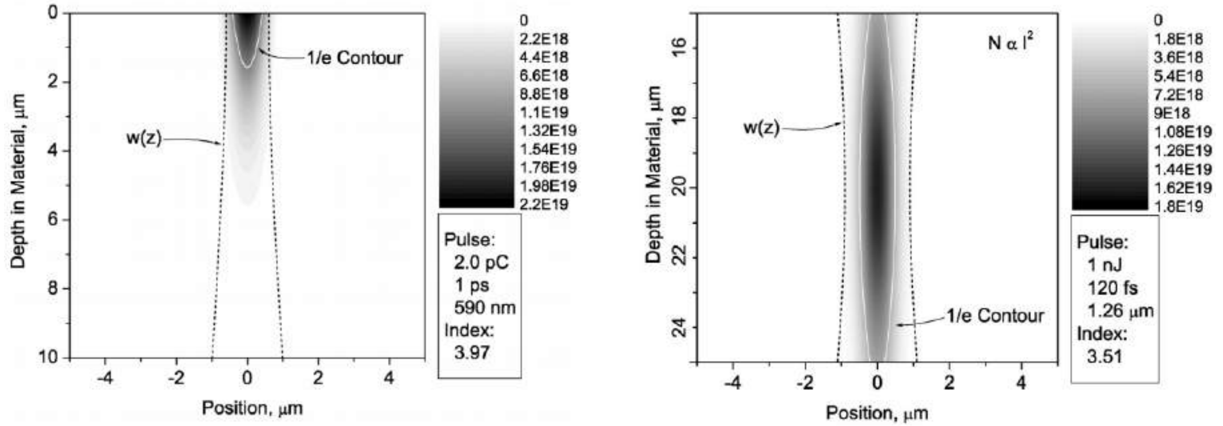

Figure 3.3: Charge density plot comparisons for an SPA process versus a TPA process [2]. The SPA wavelength used was 590 nm, while 1260 nm was used for TPA.

Firstly, the wavelength selected must be above 1,100 nm as previously mentioned. In a practical setting it is useful to choose a wavelength at least slightly longer to ensure no contributions from SPA arise. For example, the TPA wavelength used at the SSSC is 1,200 nm. Secondly, the irradiance needs to be sufficiently high. To achieve this, the spot size of the laser beam must be focused to a small area on the order of a few μm and the pulse duration must be very short, on the order of several hundred femtoseconds or less. Thus, an ultrafast pulsed laser is generally required if the TPA method is to be used. Recall that ultrafast lasers can generate extremely high peak powers due to their very short pulse duration.

According to Equation 3.9 the light is not attenuated at an exponential rate as it passes through the medium as compared to Beer's Law. As well, from Equation 3.6 the charge carrier density depends on the square of the irradiance. With these two important properties, by using TPA it is possible to inject charge at effectively any depth into the substrate by changing the position of the objective lens while also limiting the injection to the confocal region where the vast majority of the irradiance is concentrated. Figure 3.3 illustrates the differences between the charge density generation profiles between SPA and TPA. The plots indicate that the charge density decreases with depth into the material for SPA , while for TPA it is maximized at the focal point of the laser beam. The SPA and TPA processes have their own particular advantages and as such both methods continue

to be used today.

3.5 Testing Parameters Considered for SEE Evaluation Using a Pulsed Laser System

In the previous section the interaction of light with silicon in terms of SPA and TPA was described. In addition to the light absorption process in silicon there are additional parameters that must be considered for pulsed laser of testing of SEEs. These include additional properties of the pulsed laser source, optical components that affect the laser beam, and also practical considerations such as deciding whether a device should be tested using SPA or TPA. The goal of this section is therefore to discuss these primary remaining factors that can alter a device?s SEE response to a pulsed laser.

3.5.1 Single Photon Absorption or Two Photon Absorption: Front Side vs. Back Side Irradiation

As discussed, SPA and TPA differ in how the charge carrier generation occurs. As a result, a user might be left wondering which technique should be used under the presented conditions. As a general rule, SPA is often employed when the sensitive areas are located on the top/front side of the chip where they can be directly exposed to the laser without interference from packaging or metal interconnects. This is known as front side irradiation, and should be used where possible. Front side irradiation via SPA is easier to compare with heavy ion data as the calculation of charge deposited into the silicon can be much simpler than the case for TPA.

However, if the top side of the device cannot be directly accessed then the laser must be directed through the back in a process known as back side irradiation. While both SPA and TPA can be used for back side irradiation, SPA is limited in effectiveness as the wavelength selection is confined to a narrow region close to 1,100 nm due to the absorption properties of silicon; shorter wavelengths generally cannot penetrate into the substrate sufficiently far to reach the sensitive volume. As such it may be more beneficial to use TPA in many of these cases.

At the same time, the need for back side irradiation has increased as the feature size has decreased. The ongoing trend of designing denser, highly scaled devices has led to greater numbers of metal levels and interconnects that prevent laser pulses incident from the front side from reaching sensitive regions within the silicon. As well, a non-negligible amount of modern circuits are mounted using a flip chip configuration, thus preventing opening up the device and gaining access from the top in the first place. Back side irradiation via TPA allows circumvention of these issues in most cases. Figures 3.4 (a) and (b) illustrate front side vs. back side irradiation when using SPA and TPA, respectively.

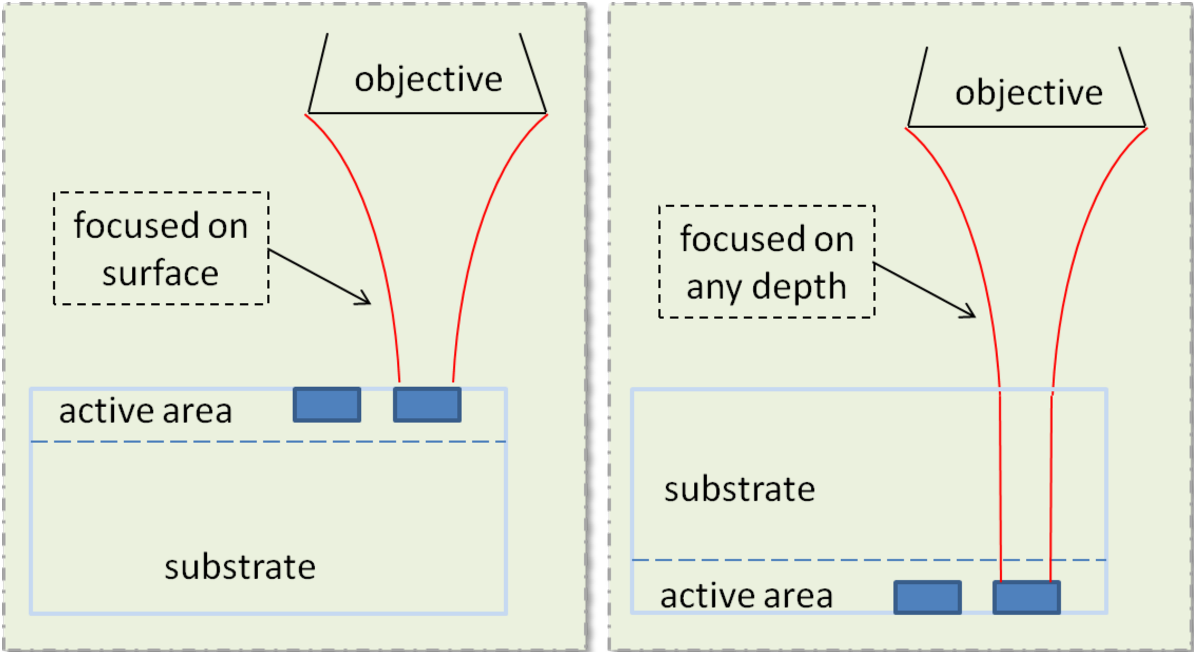

(a) Front side irradiation using SPA.

(b) Back side irradiation using TPA.

Figure 3.4: Illustration of front side irradiation and back side irradiation.

Surface Preparation for Front and Back Side Irradiation

Preparing a sample for front side irradiation is usually straightforward, often requiring nothing more than opening the package. On the other hand, preparing a sample for back side irradiation is much more involved. To expose the substrate the back cover must be removed and may require etching, grinding, chemical removal, or other processes depending on the packaging. Next, once the substrate is exposed it must be highly

polished to a mirror-like finish to ensure the beam quality is not degraded by a rough surface. Additionally, it may be desired to thin the silicon substrate by some amount so that the laser will adequately penetrate to the active areas. The time and resources necessary to prepare samples for back side irradiation is non-trivial, and users wishing to test their devices with this method must be aware of this.

3.5.2 Pulse Duration and Repetition Rate

The pulse duration of a laser can influence the SEE energy threshold of a device if it approaches or is longer than its charge collection and response times. However, as long as the pulse duration is reasonably shorter than the response time it will not have a meaningful effect on an experiment [20]. Fortunately, sub-picosecond ultrafast lasers generally do not have this complication as their pulse durations are much shorter than the response times of even the fastest modern devices and ICs.

To achieve greater flexibility in probing a device's SEE response the repetition rate of a laser system should be configurable, either by changing the settings of the pulsed laser itself or through external means. The purpose is essentially to vary the frequency at which the device under test is hit by incoming laser pulses. This is important because if a device is not able to relax to an equilibrium after being hit by a laser pulse before the next one, the measurement may be compromised. An appropriate repetition rate is also helpful in ensuring that the device being tested will receive a sufficient number of pulses in the areas being irradiated by a laser.

3.5.3 Laser Spot Size

The response of a circuit depends at least partially on the spatial profile of the laser beam. More specifically, the smallest area that can be probed on a device is dictated by the spot size, which depends on the microscope objective lens and wavelength of light used. If the laser is modelled as a Gaussian beam, then after being focused by the objective lens the minimum spot size is given by [24].

$$w_0 = \frac{2\lambda}{\pi \cdot NA} \tag{3.10}$$

where w_0 is the beam waist at $1/e^2$ of the maximum intensity, λ is the wavelength of light used, and NA is the numerical aperture of the lens. NA is defined as $NA = d/2f$: the ratio of the diameter and focal length of the lens all multiplied by one half.

As can be seen, to achieve a smaller spot size, shorter wavelengths and lenses with larger NAs should be used. Generally, a spot size as small as possible is desired so that the features in devices such as highly-scaled memories can be specifically probed without overlapping into other sensitive areas.

At the SSSC pulsed laser facility two primary objective lenses are used for testing: one with a 10x magnification and NA of 0.3, and the other with a 50x magnification and NA of 0.65. Using Equation 3.10, Table 3.1 illustrates the theoretical minimum spot sizes for both lenses at wavelengths of 580 nm and 1200 nm.

Table 3.1: Spot size calculations for the objective lenses used at the laser facility at wavelengths of 580 nm and 1200 nm.

Objective Lens	**Numerical Aperture**	**Spot Size (580 nm)**	**Spot Size (1200 nm)**
Nikon 10x	0.3	1.23 μm	2.55 μm
Mitutoyo 50x	0.65	0.568 μm	1.18 μm

Chapter 4
The Pulsed Laser Facility for SEE Testing at the Saskatchewan Structural Sciences Centre: Equipment and Setup

4.1 Background

Pulsed laser facilities have been set up around the globe to meet the needs of the radiation effects community. Some of the most well known facilities include those maintained at the United States Naval Research Laboratory (NRL), NASA's Jet Propulsion Laboratory (JPL), the European Aeronautic Defense and Space Company (EADS), and IMS in Bordeaux.

Over the past three years, through a collaborative effort between Dr. Li Chen and the Saskatchewan Structural Sciences Centre (SSSC), a new pulsed laser facility for SEE testing has been developed. Previously, Dr. Chen collaborated with the SSSC and had developed an earlier iteration of the pulsed laser facility. However, no work during the course of this thesis was performed on the old system. As well, the new setup consists of different (though functionally similar) pieces of equipment, from the laser source to the microscope. The end result has been a system that offers better spatial, temporal, and parametric functionality for SEE testing. For example, the previous system was not capable of supplying a wavelength necessary for two photon absorption.

In this chapter, the equipment setup and capabilities of the laser facility for SEE testing at the SSSC are described. Currently the only facility of its kind in Canada capable of serving the radiation effects community, the SSSC pulsed laser facility is a custom-designed setup that offers a broad range of features and wavelengths. This allows

users to test the SEE response of their devices using both single (SPA) and two photon absorption (TPA). As of the time of this writing the information presented here is up to date, however it is anticipated that the facility will change over time both to receive ongoing hardware and software upgrades as well as to meet the needs of the radiation effects community.

4.2 Facility Equipment Setup

The SSSC laser facility is shown in Figure 4.1. Consisting of multiple pieces of equipment, the system itself is divided into two main stages: an amplification stage which allows for tuning of laser power, wavelength, and repetition rate, and a post-amplification stage which includes the components of the system that manage and monitor how any devices under test (DUTs) are irradiated. The overall layout of the SSSC laser equipment in block diagram form is shown in Figure 4.2. The principles of operation of each piece of equipment will be described here.

Figure 4.1: Photo of the SSSC SEE laser facility at the University of Saskatchewan. The Verdi, Vitesse, RegA, and OPA units are shown and labelled.

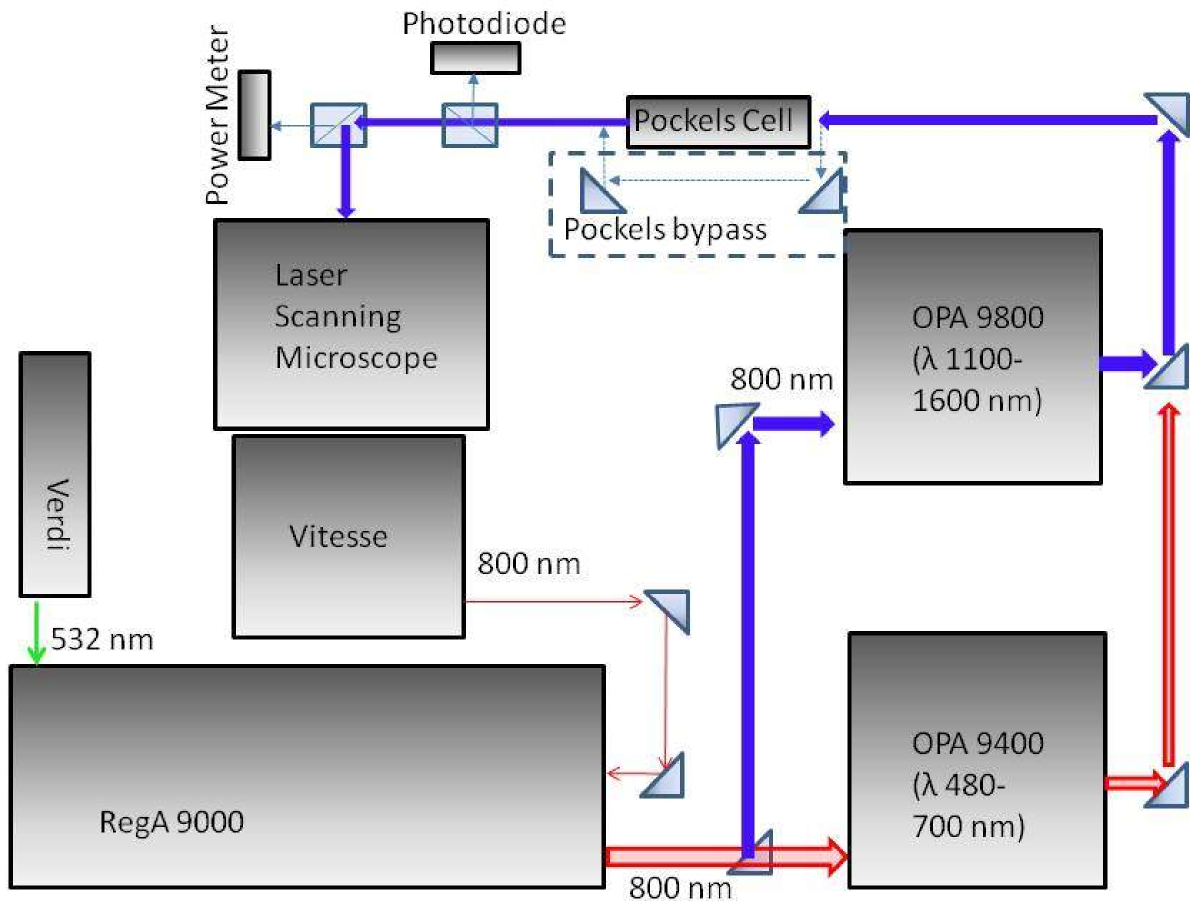

Figure 4.2: Block diagram of the SSSC SEE laser setup from a top-down view. The arrows indicate the beam paths of the lasers used.

4.2.1 Amplification Stage

The amplification stage consists of a diode-pumped solid state Nd:YVO_4 Verdi V-18 laser, Vitesse-800 mode-locked titanium:sapphire laser, and a RegA 9000 regenerative amplifier, all manufactured by Coherent, Inc. As the pump source of the RegA, the Verdi provides a continuous wave 532 nm input with power up to 18 W. However, only a maximum of 14 W is used at any time.

Simultaneously, the Vitesse provides an 800 nm pulsed laser with a pulse width of 130 femtoseconds (fs) and 80 MHz repetition rate to act as the seed laser for the chirped pulse amplification process within the RegA [25].

The chirped pulse amplification process in the RegA 9000 is relatively involved, and as such a brief explanation is presented here. First, the pump input from the Verdi passes

through a titanium:sapphire crystal in the RegA [26]. Simultaneously, the 800 nm seed input from the Vitesse passes through a Faraday isolator, then to an acousto-optic cavity dumper to inject single pulses into the remaining RegA optics. Amplified at a repetition rate of 250 kHz, these pulses perform 20 to 30 round trips within the RegA laser cavity, after which they return to the Faraday isolator and are once again extracted by the cavity dumper. They are separated from the input beam via a polarizer. Since the amplification process causes temporal broadening of the pulse duration to about 30 picoseconds, the RegA contains compressor optics to re-narrow the beam down to a value of approximately 200 fs. The resultant output is an 800 nm beam 3 mm in diameter with a pulse duration on the order of 200 fs [26]. The repetition rate of the RegA output is configurable between 10 kHz to 300 kHz which is adjusted by changing the settings in its accompanying electronic controller. The repetition rate can be lowered further through the use of an external delay generator. The RegA output can be directed via a set of flip mirrors into an OPA 9800, OPA 9400, or used directly as a source laser (not pictured in Figure 4.2). The OPA 9800 is generally used for two photon absorption due to its primary output between 1,100 nm and 1,600 nm, while the OPA 9400 is mostly used for single photon absorption.

The Optical Parametric Amplifier Model 9800 (OPA 9800) is an accessory parametric amplifier to the RegA 9000 used to generate a wavelength-tunable output. The parametric amplification starts by taking the 800 nm output RegA output and splitting it with a 75/25 beamsplitter. The beam containing 75% of the incident beam energy is sent to a dichroic mirror, while the beam with the remaining 25% is sent to a sapphire crystal which produces a whitelight continuum between 460 nm and 1600 nm [27]. The whitelight passes through an optical delay known as the first pass delay on its way to combining with the 75% energy beam at the dichroic mirror. Both beams then pass through a beta barium borate (BBO) crystal for the first time. The resulting output is a residual 800 nm beam as well as small amounts of signal and idler output. The signal output is separated from the 800 nm beam through a second dichroic mirror and sent to a fixed optical delay. At the same time, the 800 nm beam is sent to a second optical delay (second pass delay) which is then recombined with the signal at the second dichroic mirror for a second pass through the BBO crystal. The end results are a primary signal between 1,100 nm and

1,600 nm, an idler signal between 1,600 nm and 2,400 nm, and the residual 800 nm signal. The output wavelengths can be tuned by adjusting the external micrometers attached to the BBO crystal mount and first and second pass delays. These change the angles of the crystals upon which the beams are incident as well as the timing of their convergence within the BBO crystal. The operation of the OPA 9400 is nearly identical, but contains a second BBO crystal to frequency double the 800 nm input down to 400 nm.

4.2.2 Post-Amplification

After amplification of its power and parametric properties, the laser is passed through two more significant apparatuses: the Pockels cell and the microscope. For simplicity, in this section it is assumed that the primary output signal from the OPA 9800 is used. However, the discussion is general and can be applied to the other beam outputs as well.

As shown in Figure 4.2, after exiting the OPA 9800 the beam is passed to a Conoptics Model 360-40 electro-optic modulator, or Pockels cell. This model can take wavelengths between 680 nm and 1300 nm. Thus, most of the wavelength range of the OPA 9400 is cut off and cannot take advantage of the Pockels cell. As also shown in Figure 4.2, it can be bypassed by using mirrors if desired. Interfacing with the microscope and software, the Pockels cell provides the user with increased spatial and temporal selection over laser irradiation parameters. It essentially acts as a high end switch to modulate the beam at certain positions and time intervals to irradiate a sample under the microscope according to the user-specified input.

After passing through the Pockels cell, the beam goes through an optic that sends approximately 3% of the power to a ThorLabs DET10C fast photodiode connected to an oscilloscope. This allows users to monitor changes in the laser pulse stability during testing. From there the beam passes through a 90/10 beamsplitter, sending 90% of the beam to the microscope and the remaining 10% to a Coherent OP-2 IR power meter which measures the average power of the beam.

To measure the power of the pulsed laser directly at the stage, a handheld ThorLabs S132C power meter is available. This model of power meter is slim, and as such the power coming out of the objective lens can be measured by placing it between the lens and the

sample. Care must be taken to ensure the user does not bump the sample during the power measurement, but with a little bit of practice this procedure is relatively easy.

The microscope used by the laser facility is a ThorLabs MPM200-SGP paired with a ThorLabs height-adjustable PHYS24-m stage. The setup is pictured in Figure 4.3. It can be moved in all three directions using the knobs on its base. Until very recently, the microscope was only motorized in the vertical z direction but with the addition of a new controller the x and y directions are fully motorized as well. As a result, all three directions can be adjusted in steps as fine as 0.1 μm using the ThorLabs software.

By design, the stage that the samples are mounted on is fixed. Instead, to achieve movement in the x, y, and z directions, the microscope column is designed to vary its position. This approach has several important advantages. It allows for fast scanning over the entire sample, offers high resolution, and avoids problems arising from stage hysteresis.

Figure 4.3: Photo of the ThorLabs MPM200-SGP microscope and stage. The 50x objective lens is also visible in the picture.

To enter the microscope the beam first passes through a periscope then up to a beam-splitter and into the galvanometer motorized mirror assembly (”galvos”) which is respon-

sible for scanning the position of the beam in the x and y directions within the field of view. The following section will elaborate on this process further. After the galvos the beam passes through a fisheye lens that expands the focused spot onto a mirror which bounces the beam downwards onto the back of the objective lens. The overfilled lens focuses the light into a tight beam spot (typically on the order of 1-3 μm in diameter depending on the objective) on the sample for testing. The microscope is then connected to a PC via a ThorLabs electronic control unit (ECU).

4.3 Laser Irradiation Procedures

In this section the various parameters that dictate how devices under test (DUTs) can be exposed to laser irradiation are described, and a description of the software features are also provided. Using the ThorImageLS program on the PC, the user is able to specify various parameters the microscope uses when a sample is being irradiated.

A useful feature of the laser system is the ability for a user to view a DUT in real time as the device is subjected to laser pulses. To accomplish this, a continuous wave Mitsubishi ML725B8F 1310 nm imaging laser is connected to a port on the side of the microscope. The imaging laser then travels along the same optical path as the pulsed laser starting at the last beamsplitter within the microscope. Interfering non-destructively with the sample, an image is collected using the back reflection as collected by the objective and passed back through the galvos and dichroic to a ThorLabs PDA20CS detector. After overlapping the two beams it is possible to accurately probe the desired test areas by finding the region of interest on the sample based on the image provided by the software. ThorImageLS displays and continuously updates this image for the user.

For the irradiation of a device, the most straightforward method is to perform a continuous scan of the area within the field of view. In this mode, the microscope galvos continuously sweep the pulsed laser across the field of view. The amount of time the galvos spend idling on each pixel is known as the dwell time and can be changed in ThorImageLS. It is also possible to digitally zoom in on the image if the user wants to only irradiate a specific area. The galvos respond to a digital zoom by tightening their scan range so that only the area seen in the image is still hit by the pulsed laser.

As the laser facility has received ongoing software and hardware upgrades, it is now possible for the user to draw regions of interest (ROIs) on the image to irradiate specific areas accordingly. The primary irradiation parameters of concern to the user include the pixel density, dwell time for each pixel, scan pattern, and number of times to iterate the scan over the ROI. While the user has some flexibility in creating a polygon shape of their choice, the most useful types of ROIs to use for device testing are often the rectangular and single point tools. These types are discussed here.

The user creates a rectangular ROI by simply selecting the appropriate tool in software, then clicking and dragging to create a box with the desired dimensions. The galvos are then programmed to scan through that area with the specified parameters. Working in parallel with the galvos, the Pockels cell delivers the desired laser power inside the ROI and drops the power to the minimum passable power when the galvos travel outside the ROI. Figure 4.4 shows an image of the configuration memory of the Virtex-5 FPGA with a rectangular ROI selected.

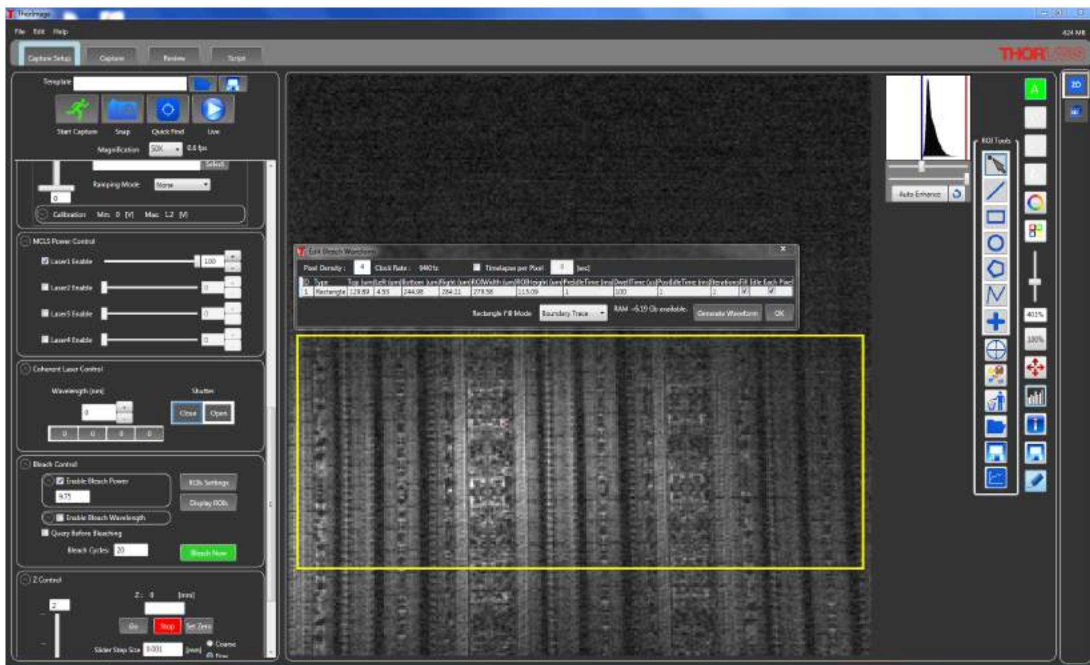

Figure 4.4: Screen capture of the ThorImageLS software version 2.3 with a section of the Virtex-5 configuration memory being imaged by the imaging laser. The yellow box is the rectangular ROI selected.

The single pixel ROI is used to select exactly one pixel on the image for irradiation.

Represented by a colored crosshair, the single pixel, or point ROI is an especially powerful tool as it allows users to inject exactly one or multiple laser pulses into their devices with the spatial resolution only limited by the minimum beam spot size. Figure 4.5 depicts a DUT with a point ROI. Additionally, note the red areas in Figure 4.5. These areas represent oversaturation of the pixels on the detector receiving the signal from the imaging laser; they do not represent hotspots sensitive to SEEs. Rather, this phenomena is often caused by highly reflective components or areas on the device such as metals.

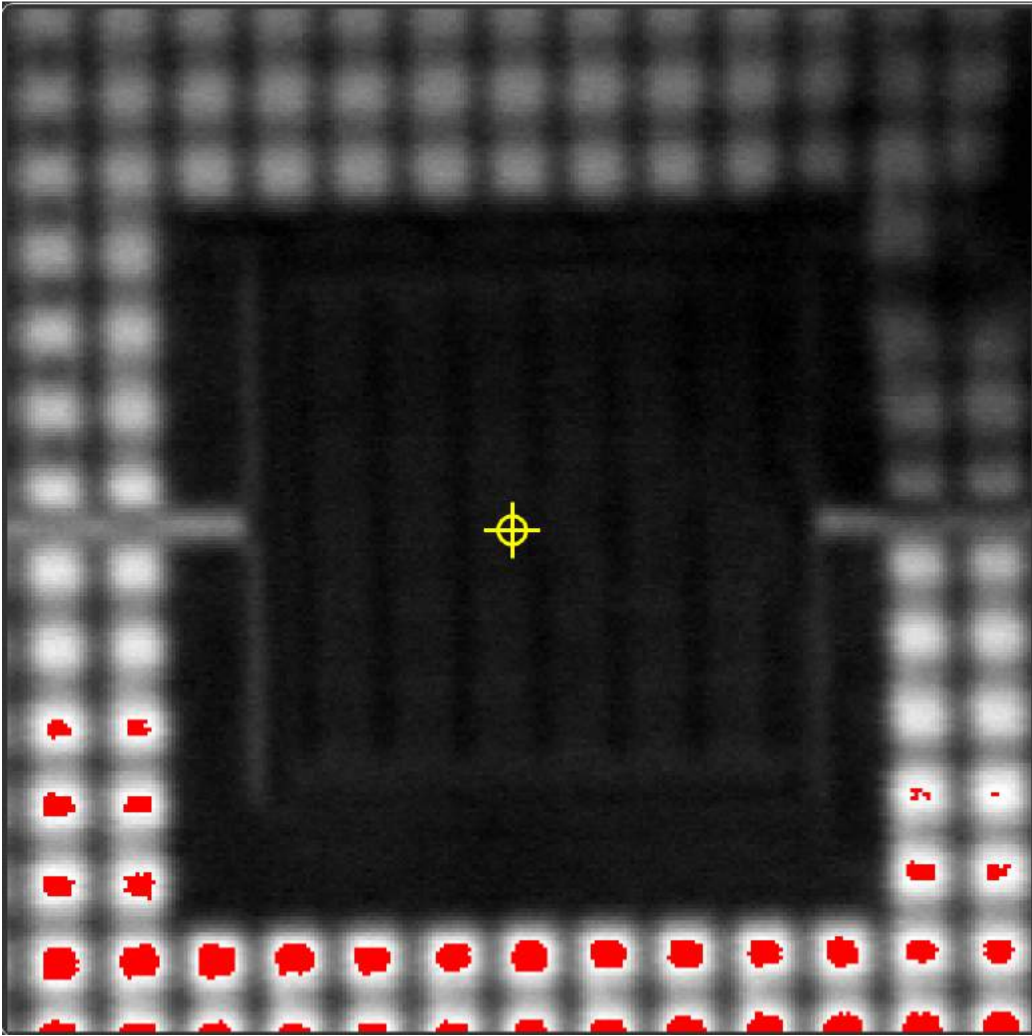

Figure 4.5: Point ROI on a DUT. The yellow crosshair indicates the sole location where incoming laser pulses will be injected.

Overall, the new ability to draw ROIs on screen and specifiy the irradiation parameters to a greater precision is a very useful addition to the system.

Chapter 5
Response of Optek OMH3075 and Infineon TLE4945 Hall Effect Sensors to Single Event Effects Induced via Single Photon Absorption

5.1 Introduction

A Hall effect sensor (HES) is a type of transducer that responds to magnetic field strength with a varying output voltage. They are used in applications for non-contact proximity switching, positioning, speed detection, and current sensing, among others [28]. One example is an electric motor tachometer. In fact, they also found application in space. HESs manufactured by Micropac Indsutries, Inc. were used in mechanisms of the Mars Science Lab Mission [29]. As well, one of the models studied here, the Infineon TLE 4945, is proposed for use on the European Space Agency's (ESA) ExoMars rover. The intended use is as a component in the brushless DC motors for the rover's drilling and sampling mechanism [30]. Any HESs used on a Mars mission will be exposed to radiation environments both in space and on the Martian surface. Therefore, it is useful to characterize their response to single event effects (SEEs) and total ionizing dose (TID).

Sanders et al. evaluated the TID and heavy ion SEE response of an Optek OMH3075 HES [31][32] while Phillips *et al.* evaluated the TID response of an Infineon TLE4945 HES [30]. As both of these HES models have been qualified as candidates for potential use in space applications, a unit of each was procured by MDA Corporation for pulsed laser testing at the University of Saskatchewan. The goal was to observe and compare

the single event transient (SET) responses of these sensors, both with each other and the available data.

As of the time of this writing and to the best of our knowledge SEE data is not available for the Infineon HES and no laser SEE data is available for the Optek HES. Further evaluation of the SEE response of these sensors is recommended. In this chapter, single photon absorption (SPA) pulsed laser irradiation results for the Optek and Infineon HESs are provided. The results show the locations of the SEE sensitive regions of each sensor, compare laser SEE performance of each sensor, and are compared to the available published heavy ion data [31][32]. Therefore, the results given here represent the first evaluations by a pulsed laser of these HES models. They also represent the first use of SPA to evaluate device response for the new laser setup at the SSSC pulsed laser facility.

5.2 Overview of Sensors

As previously mentioned, the HESs evaluated are the Optek OMH3075 and Infineon TLE4945. Figures 5.1 and 5.2 show the block diagrams of the Infineon and Optek devices, respectively. As can be seen, the Infineon model consists of a Hall generator, threshold generator, operational amplifier, and Schmitt-trigger. If a magnetic field is applied, the Hall probe will develop a voltage. This voltage is amplified and transferred to the output pin through a Schmitt-trigger. The sensor has built-in temperature compensation circuitry which allows for operation over a wide temperature range. The Optek sensor functionality is similar. Included on both chips is a band gap voltage regulator that allows operation over a wide range of supply voltages. Table 5.1 shows the extreme operating voltage ranges of each device.

Table 5.1: Minimum and Maximum Operating Voltage of OMH3075 and TLE4945 devices.

Model	V_{min}	V_{max}
Optek OMH3075	4.5	24
Infineon TLE4945	3.8	24

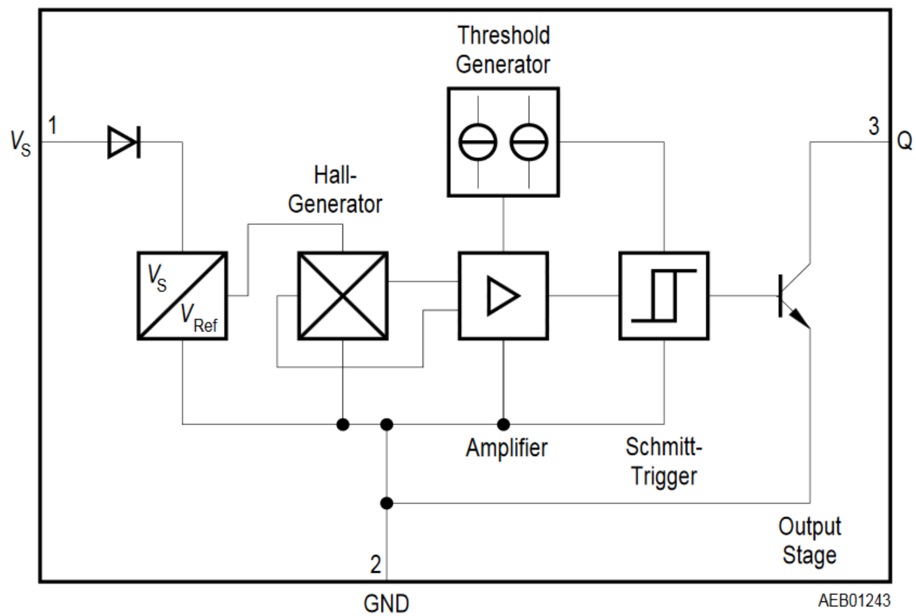

Figure 5.1: Block Diagram of Infineon TLE4945 HES [3].

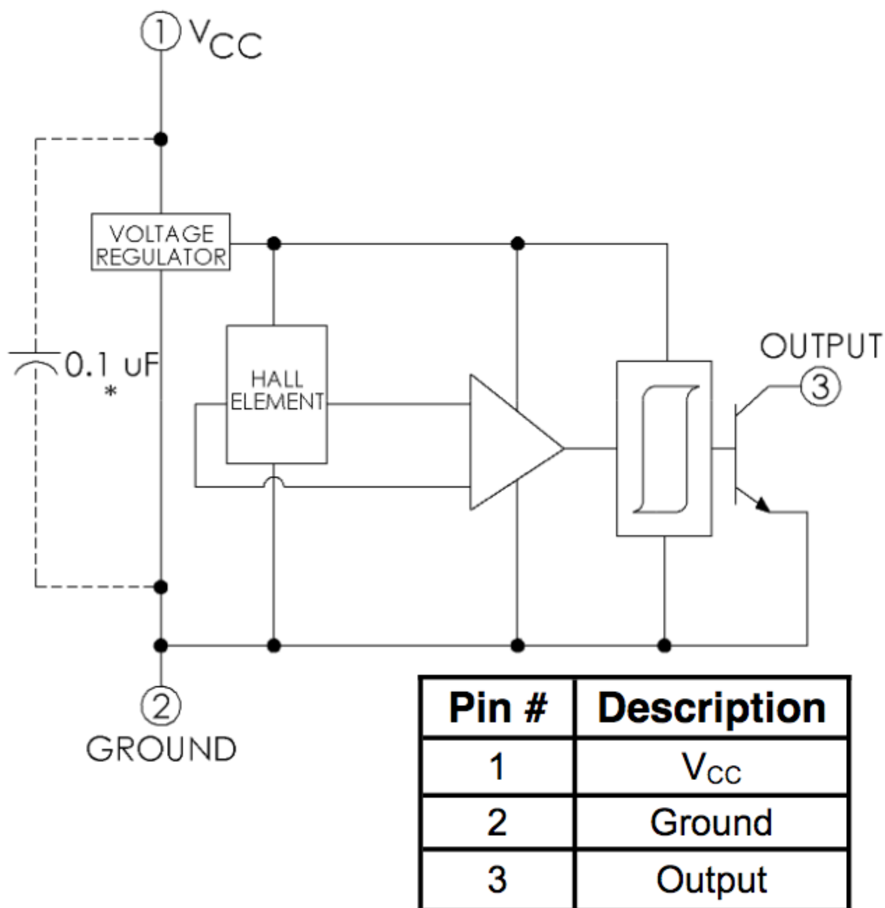

Pin #	Description
1	V_{CC}
2	Ground
3	Output

Figure 5.2: Block Diagram of Optek OMH3075 HES [4].

5.3 Test Facility

Pulsed laser testing was conducted at the Saskatchewan Structural Sciences Centre (SSSC) at the University of Saskatchewan; the equipment was previously described in Chapter 4.

The use of pulsed lasers has been adopted by the radiation effects community both as an alternative and supplement to high energy particle irradiation. As discussed in previous chapters, pulsed laser-based SEE testing maintains several advantages over broad beam, high energy particle irradiation. Some of these include control over the timing and location of the photoelectric interaction between the laser and the material, as well as no accumulation of ionizing or displacement damage dose. However, microelectronic devices are not impervious to laser-induced damage. Therefore, thermal degradation and protection against the possibility of destructive latchup must still be considered [33].

5.4 Experiment Setup

As the active areas for both HESs can be exposed directly to the air after being de-lidded, it was decided that the SEE sensitivity would be evaluated using the SPA mechanism. By choosing an appropriate wavelength this was accomplished. Due to the front-facing design, it was not necessary to focus through a substrate to observe the layout of the device. The OPA 9400 was configured to give an output wavelength of 580 nm, and the resulting output beam was aligned into the microscope. Table 5.2 lists the primary laser and objective lens properties used during the testing of the HESs.

Table 5.2: Laser Irradiation Parameters for Hall Effect Sensor Studies.

Wavelength (nm)	**Objective Lens**	**Repetition Rate (kHz)**	**Pulse Width (fs)**
580	10x with 0.3 NA	10	200

During our testing, a laser wavelength of 580 nm with a repetition rate of 10 kHz was used, which is the lowest rate that the RegA 9000 can output natively. It was not possible to use the Pockels cell for this experiment as the lowest wavelength it is rated for is 680 nm while 580 nm was used. Therefore the Pockels cell was bypassed and the

only irradiation method available was the continuous scan mode over the region within the field of view in the ThorImageLS software. A dwell time of 5.2 μs per pixel was used. To achieve the wavelength necessary, the output beam from the RegA was passed through the OPA 9400.

The Optek and Infineon devices were mounted onto two separate prototype boards. MDA Corporation in Brampton designed, soldered, and supplied these custom boards for use for laser testing. MDA also properly de-lidded the sensors so that their front-facing active areas could be directly exposed to the laser. The boards themselves are nearly identical in their layout; both contain a solenoid to produce the required magnetic field. Each board also provides five electrical connections: voltage supplies to the solenoid and HES, as well as a signal output from the HES for connecting to an oscilloscope. A block diagram of the test board is shown in Figure 5.3 and photos of the boards are given in Figures 5.4 (a) and 5.4 (b).

To measure the power delivered to the devices at the stage, a Coherent OP-2 VIS model sensor was available. To ensure optimal accuracy, all power measurements were taken in as dark of an environment as possible by shutting off all the major light sources in the room including fluorescent lighting, computer screens, etc.

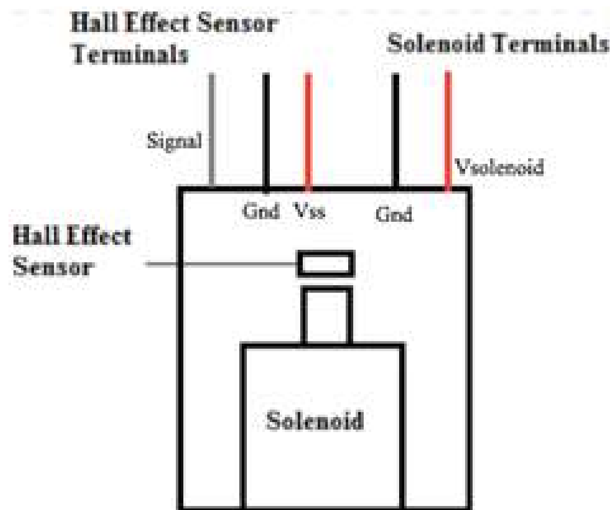

Figure 5.3: Block diagram of the test board for the Optek and Infineon HESs.

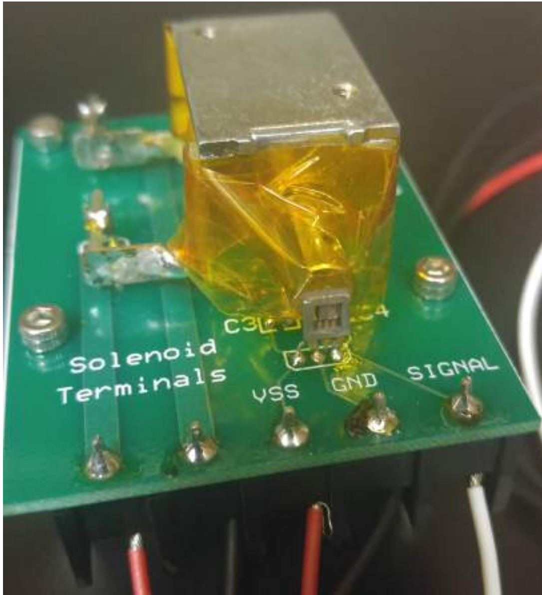

(a) Optek OMH3075 board.

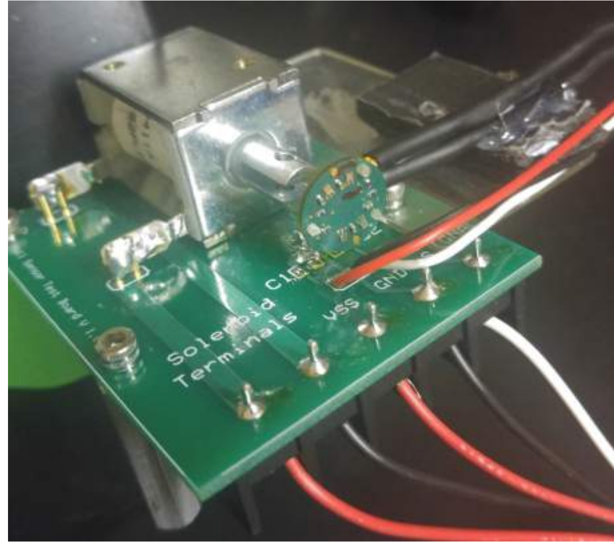

(b) Infineon TLE4945 board.

Figure 5.4: Photos of the test boards for the Optek and Infineon HESs. The device under test for (b) is indicated by the black marker lines around its area.

Both HES models are bipolar. Therefore, applying a magnetic south pole turns on a device (logic level 0 or ”low”) while applying a magnetic north pole turns off the device (logic level 1 or ”high”). However, to avoid potential confusion for the rest of the chapter, the sensor states are described in terms of being in either a high or low output voltage state. For the practical setup, applying a positive voltage to the solenoid creates an output logic low state for the HES, while applying a negative voltage sets the sensor to an output high state.

5.5 Test Conditions

Table 5.3 lists the four bias conditions under which each device was tested. 10 V was applied to the sensor in all cases. $\pm$10 V was applied to the solenoid in the first two cases, while in the last two the magnetic field was removed after inducing the device into either a high or low state. It is important to observe the output of the HES without the magnetic field present to determine the variation in SEE/SET susceptibility. If the variation is sufficiently large then reliable operation of the component providing the magnetic field is also essential to mitigate against SEEs in the HES itself.

Table 5.3: Test bias conditions.

V_{sensor} (V)	$V_{solenoid}$ (V)	Magnet Presence	Sensor Output
10	10	Yes	High
10	-10	Yes	Low
10	0	No	High
10	0	No	Low

5.6 Test Objectives

The primary test objective was to determine the SET behavior of each HES with an SPA pulsed laser while varying the laser power and to find the locations of the sensitive regions of each sensor. As such, the active areas for both the Optek and Infineon sensors were completely scanned by the pulsed laser source. In parallel with testing for SET response, any observations of either device experiencing a latchup condition to a high current state (SEL) were to be reported if found. The laser SEE results are then compared for each device and with the available heavy ion data, providing correlation between heavy ion and laser data. Recall that no SEE data is currently available for the Infineon model, and so the only comparison in this case is with the laser SEE data for the Optek model. The suitability for space applications of these sensors will also be discussed. The available energy per pulse range over which the devices were tested was between 15 pJ and 1.75 nJ per pulse.

5.7 Experimental Results: Optek Hall Effect Sensor

After scanning the entire active area of the Optek HES, several SET hotspots were found. Figures 5.5 (a) and (b) show the view under the microscope of the regions most sensitive to laser pulses according to the state the HES was initially set to.

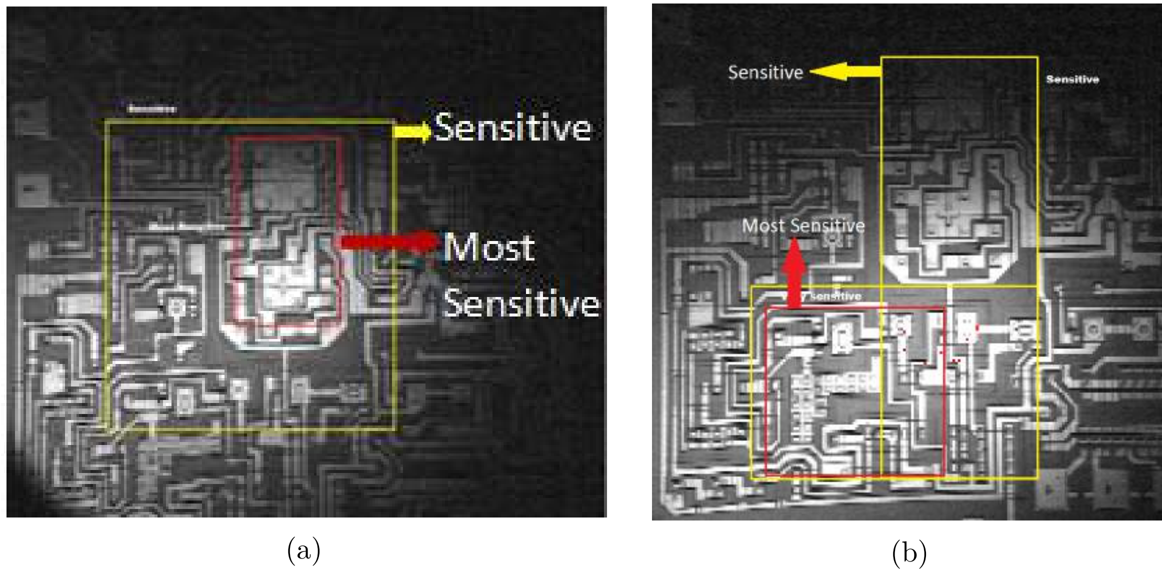

(a) (b)

Figure 5.5: Optek HES sensitive areas for the output logic high and solenoid on. (a) represents the areas most sensitive when the device started in the high states, while (b) represents those most sensitive when started in the low states.

More specifically, the exact structures that were most sensitive to SET were able to be pinpointed by zooming in and scanning over them. They are shown below in Figure 5.6 (a) and (b). 5.6 (a) is the band gap voltage reference structure for the Optek device and 5.6 (b) shows the Schmitt trigger.

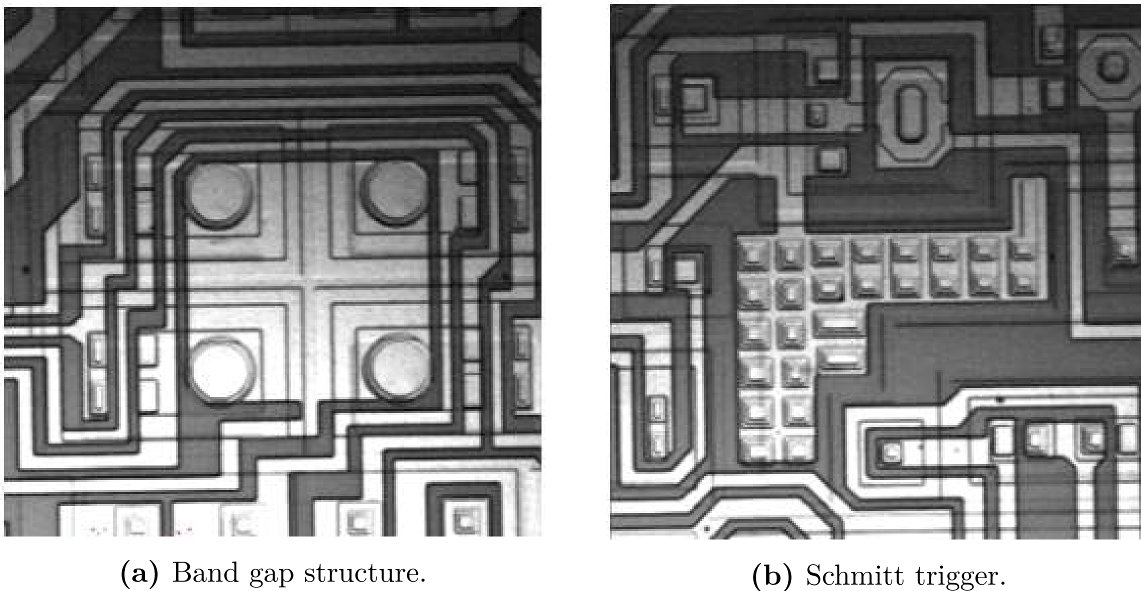

(a) Band gap structure. **(b)** Schmitt trigger.

Figure 5.6: Structures most sensitive to upset from the laser pulses. (a) is most sensitive for the high state condition, while (b) is most sensitive for the low condition.

The following laser irradiation results presented are the worst-case results from each of these structures.

5.7.1 Output Logic High and Solenoid On Test Condition

Starting the sensor in the high state with the magnetic field present, the laser threshold energy was found to be 250 pJ per pulse. Figure 5.7 shows the typical response to the laser-induced voltage output transient pulse observed. The rise and fall times are approximately 700 ns and 86 ns, respectively. The full width at half maximum (FWHM) transient pulse width is ∼900 ns, which was observed to vary slightly depending on the laser energy and area hit.

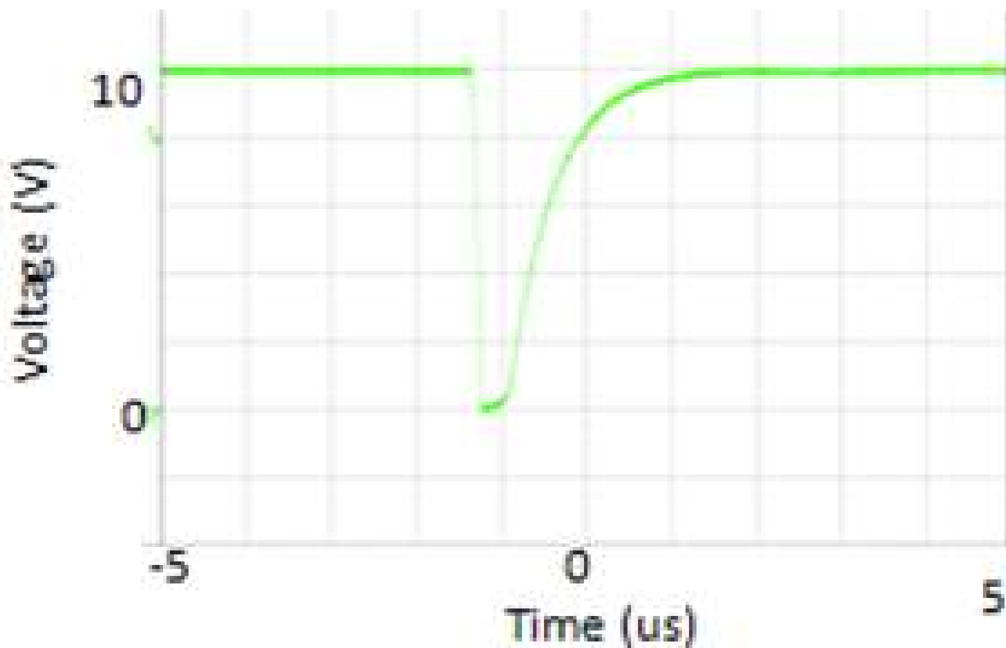

Figure 5.7: Optek HES output transient pulse observed at 250 pJ for output logic high and solenoid on.

5.7.2 Output Logic Low and Solenoid On Test Condition

Under these conditions, the output voltage is logic low. The laser was used on the sensitive structure from Figure 5.6 (b). Compared to the previous conditions, it was found that the laser pulse energy had a larger effect on the FWHM pulse width. SET output was

first observed at 635 pJ per pulse, shown in Figure 5.8. In this case, the device did not fully transition into the high state.

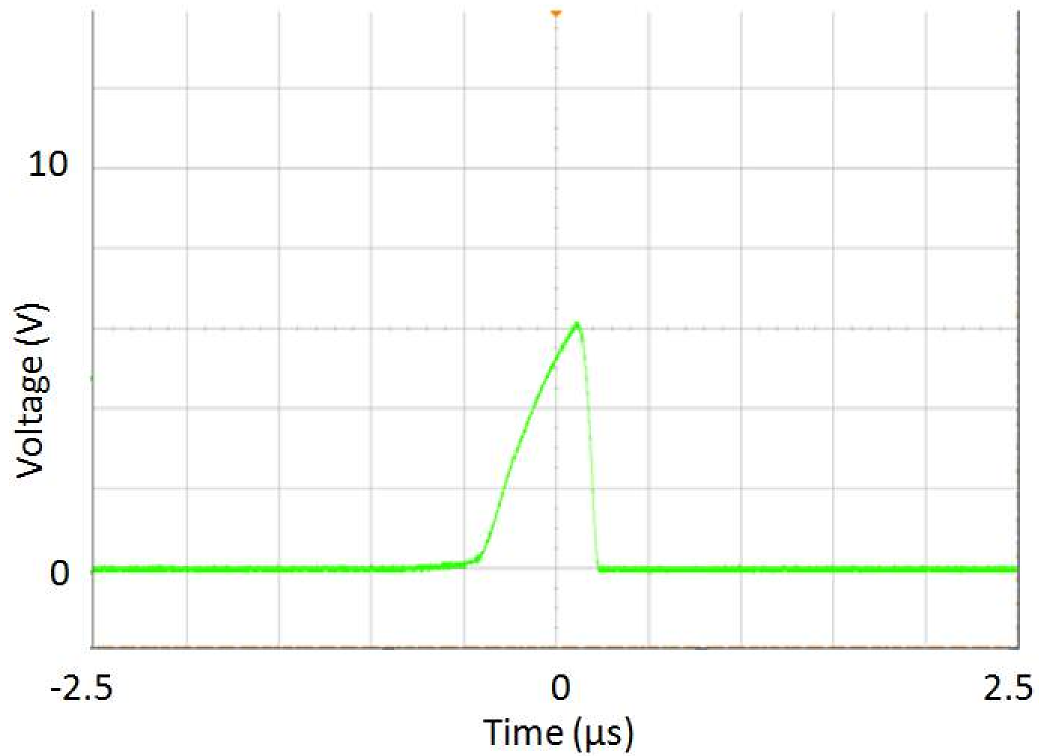

Figure 5.8: Optek HES output transient pulse observed at 250 pJ for output logic high and solenoid on.

True upset into the high state was first found at 1.15 nJ per pulse and is shown in Figure 5.9 Rise and fall times are approximately 760 ns and 60 ns, respectively. The FWHM transient pulse width is approximately 10.2 μs.

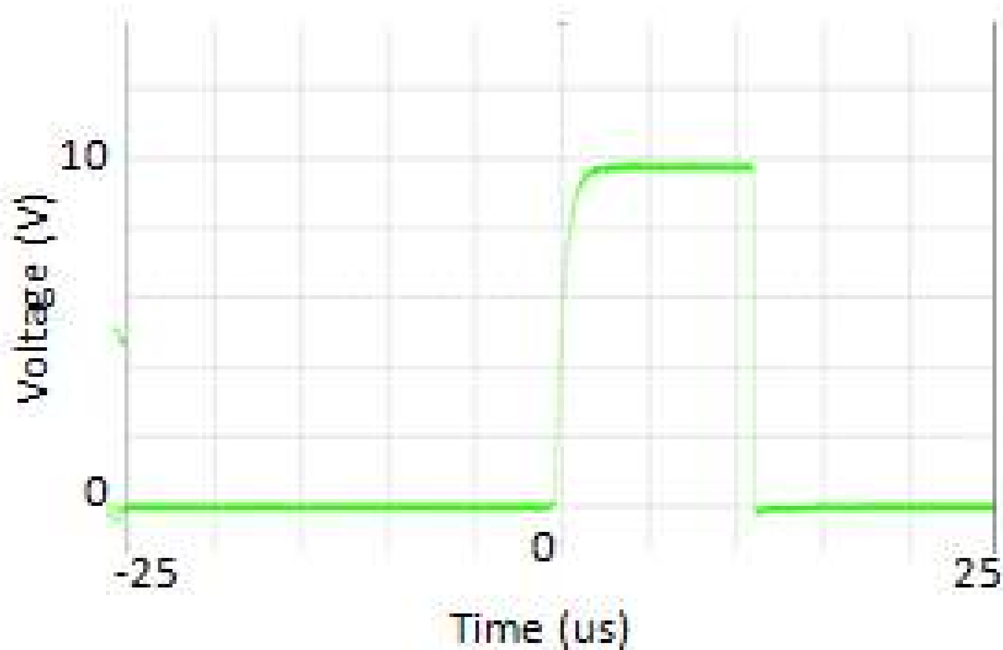

Figure 5.9: Optek HES output voltage transient observed at 1.15 nJ for output logic low and solenoid on.

The duration over which the HES could be induced into the high state was observed to increase with increasing laser pulse energy. Figure 5.10 shows the waveform at the maximum available energy of 1.75 nJ per pulse. In this case, the FWHM increased to ~11.9 μs and the rise and fall times increased slightly to 800 ns and 100 ns respectively.

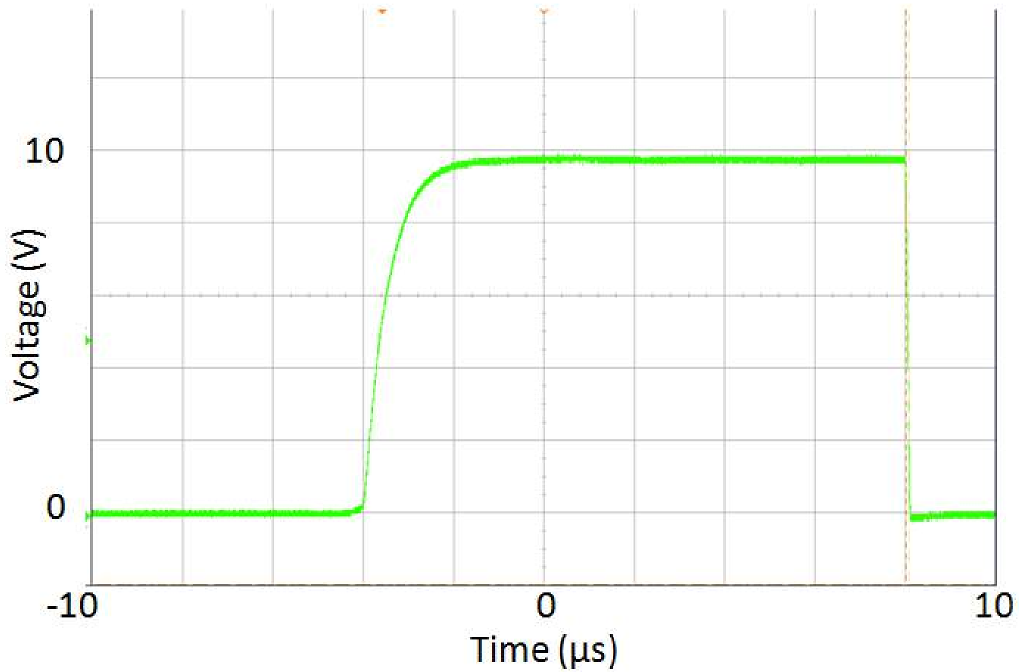

Figure 5.10: Optek HES output voltage transient observed at 1.75 nJ for output logic low and solenoid on.

5.7.3 Output Logic High and Solenoid Off Test Condition

When the applied voltage (and thus the magnetic field) was removed from the solenoid, the sensor output did not permanently stay at a logic low state when irradiated with the laser. Instead, a toggling effect occurred as the states of the output altered between logic low and high. As the results varied with some randomness, a sample waveform is shown in Figure 5.11. The durations of the low and high state are not a constant. However, they were found to always be a multiple number of the laser repetition rate of 10 kHz which has a period of 100 μs. It indicates that the changing of the states was triggered by the incoming laser pulses. Threshold for this upset was found to be 20 pJ per pulse. Additionally, the device could not be induced into staying permanently in the low state as the pulse energy was increased.

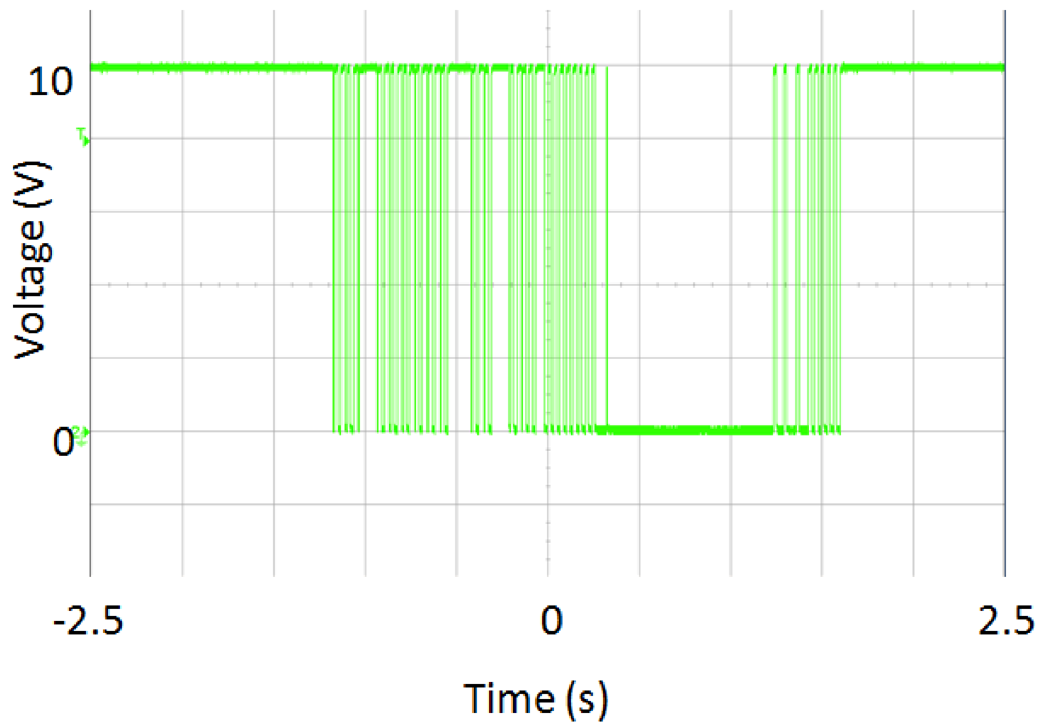

Figure 5.11: HES output voltage observed at 20 pJ per pulse for the initial output logic high without the applied magnetic field from the solenoid.

5.7.4 Output Logic Low and Solenoid Off Test Condition

Starting in the low state with no applied magnetic field, the sensor permanently remained in the high state when irradiated with the laser, as illustrated in Figure 5.12. After the magnetic field was reapplied without being irradiated by the laser, the sensor would return to its original low state. Threshold for this occurred at ~1.075 nJ per pulse.

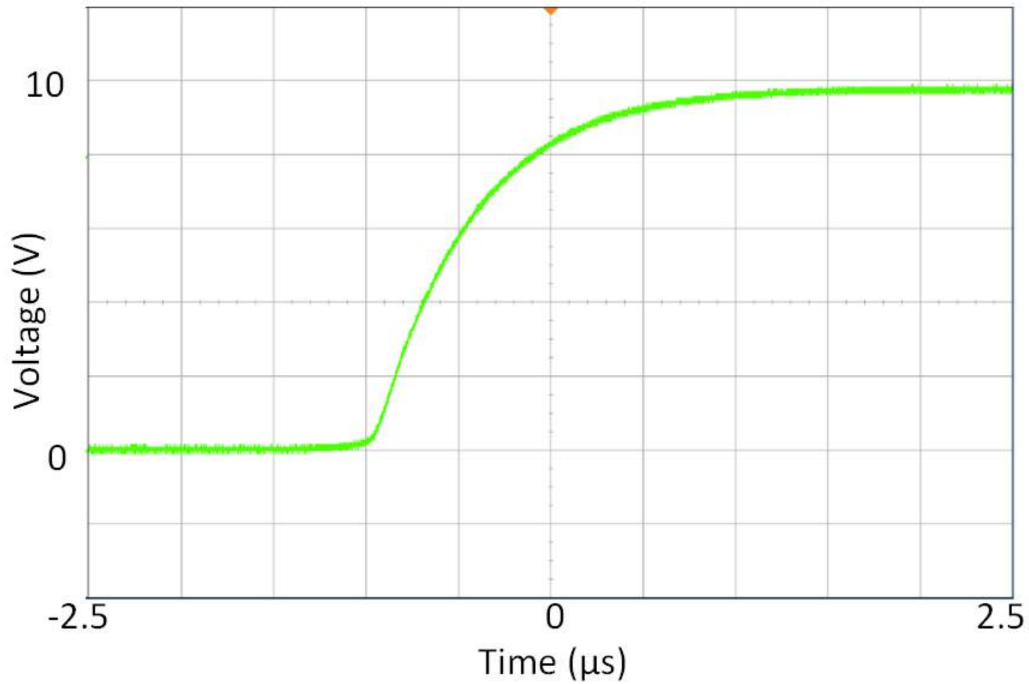

Figure 5.12: Optek HES output voltage observed at 1.075 nJ when the output starts at a logic low state without the magnetic field applied.

5.8 Experimental Results: Infineon Hall Effect Sensor

The Infineon HES was irradiated under the same conditions as the Optek HES described in Table 5.3. The entire area of the sensor was also scanned to identify potential SET hotspots. The view of the Infineon HES structure under the microscope is shown in Figure 5.13. Recalling the discussion from Chapter 4, note the red areas indicating oversaturation of the pixels on the detector connected to the imaging laser, they do not represent hotspots sensitive to SEEs.

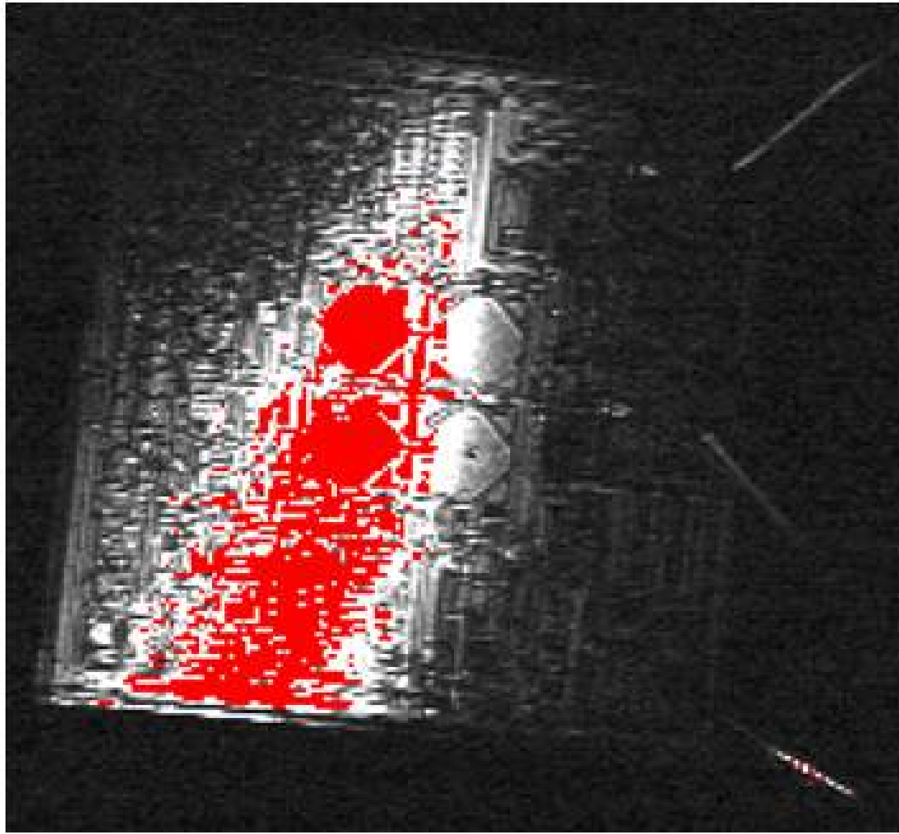

Figure 5.13: HES structure. The red areas indicate oversaturation of the image detector pixels.

Only one sensitive area, located in the center of the device and shown in Figure 5.14, was identified. Similar to the Optek HES, this structure was also concluded to be the band gap voltage reference component of the circuit. Thus, testing for the Infineon device was performed on this area.

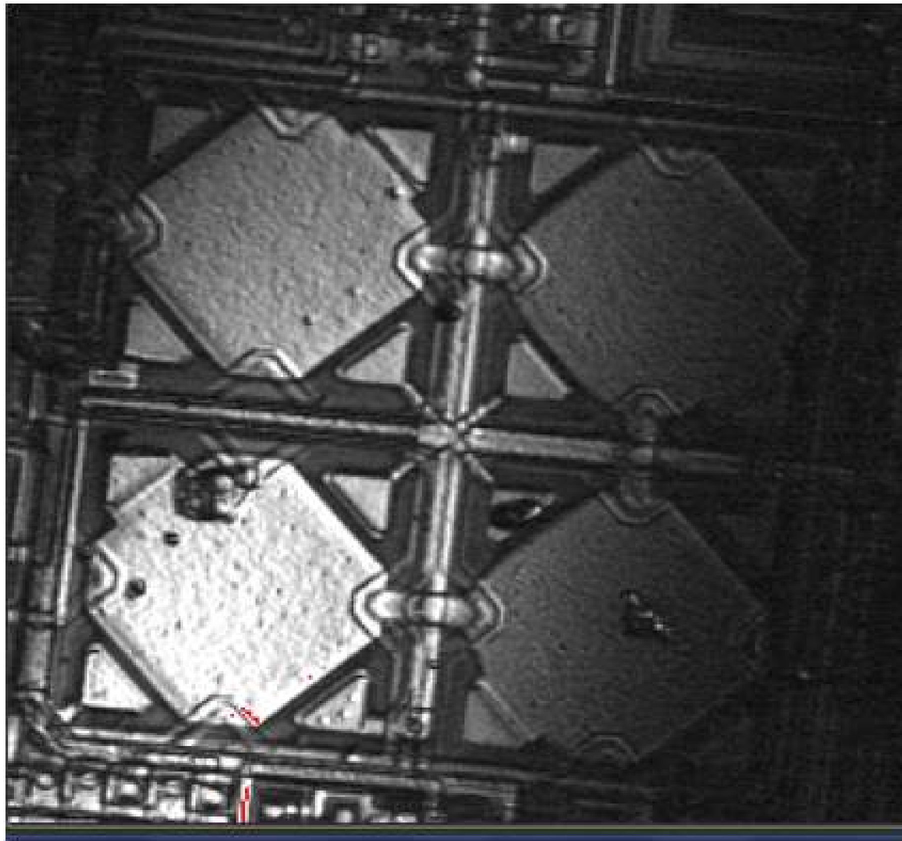

Figure 5.14: Infineon HES sensitive area.

5.8.1 Output Logic High and Solenoid On Test Condition

As can be seen from Figure 5.15, the laser threshold energy was found to be as low as 20 pJ per pulse. The transient pulse has rise and fall times of 750 and 25 ns, respectively, with an FWHM transient pulse width of 820 ns. These values are comparable to those found for the Optek HES.

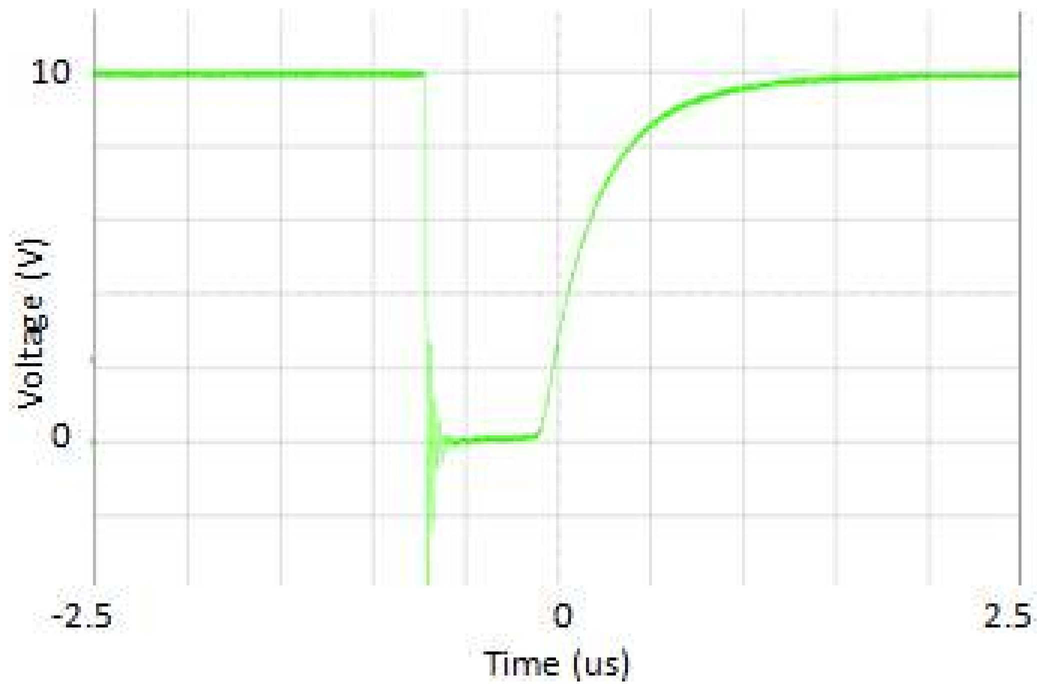

Figure 5.15: Infineon HES Output transient pulse observed at 20 pJ for the output logic high and solenoid on.

5.8.2 Output Logic Low and Solenoid On Test Condition

With the Infineon HES initially set in the low state with the solenoid on, transient behavior in the Infineon HES was observed as low as 20 pJ per pulse. However, the maximum FWHM pulse width amplitude of 1.60 μs was not observed until a pulse energy of 415 pJ was reached. This is shown in Figure 5.16. The rise and fall times were 800 ns and 25 ns, respectively.

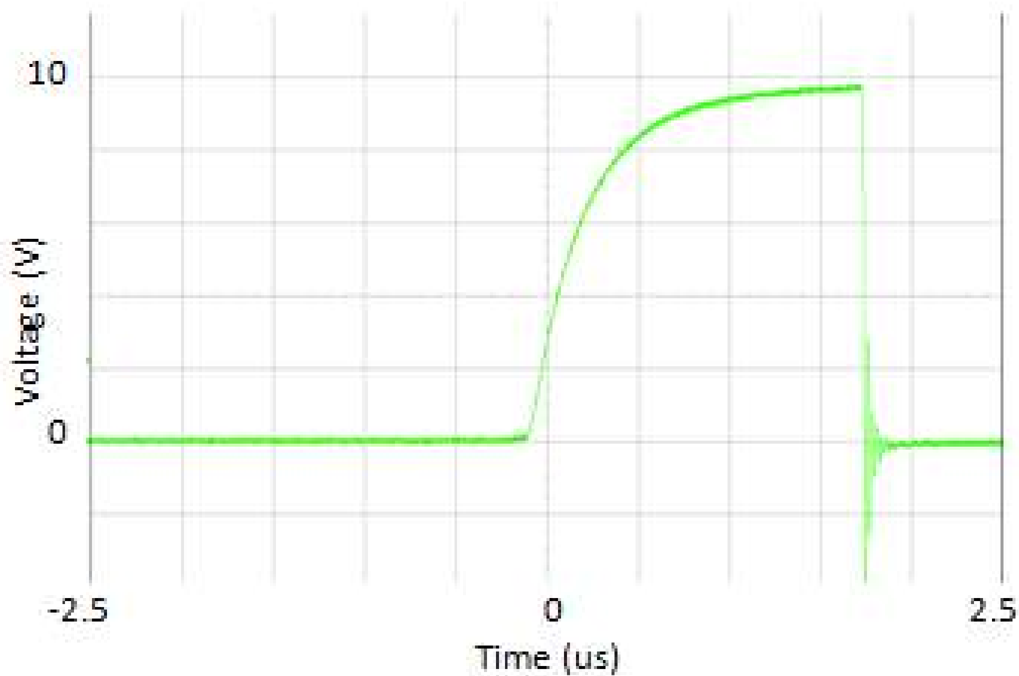

Figure 5.16: HES output transient pulse at 415 pJ, for output logic low and solenoid on.

5.8.3 Output Logic High and Low with the Solenoid Off Test Condition

When the Infineon HES started in the high state and the magnetic field was removed, the behavior was similar to the Optek HES in that the sensor output did not permanently stay in the logic low state when irradiated with the laser. As before, the sensor toggled between logic low and logic high as it was hit with laser pulses. The Infineon HES exhibited identical behavior when starting in the logic low state, the waveform for which is shown in Figure 5.17. Threshold for observing this upset occurred at a laser pulse energy of 20 pJ. Unlike the Optek HES, the Infineon HES was not observed during testing to permanently latch into a high state when the solenoid was off.

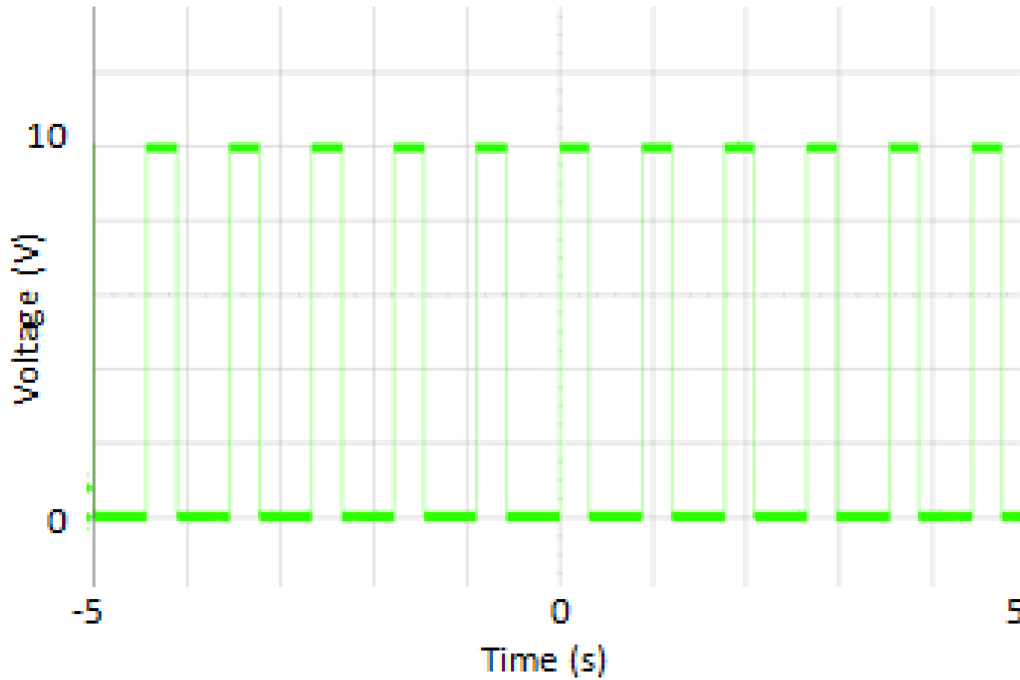

Figure 5.17: Infineon HES output voltage transient at 20 pJ for logic low or high with the solenoid off.

5.9 Discussion

With a magnetic field applied to the Optek HES, single event transient responses at the sensor's output were observed when irradiated with the laser. In both cases with an applied magnetic field, the waveform shapes and profiles produced by the laser pulses replicated those found in heavy ion testing by Sanders *et al* [31][32]. However, the FWHMs of the transient waveforms between the laser and heavy ion results are different. The laser results showed shorter FWHMs than the heavy ion results. For the sensor starting in the high state, the FWHM was 0.9 μs for the laser while the heavy ion results showed an FWHM of 6 μs [32]. For the low state the laser results gave an FWHM of 11.2 μs, and the heavy ions gave 14 μs [32]. In this case the FWHM magnitudes are more comparable. However, if more power from the laser was available at the time of testing it might have been possible to achieve an FWHM closer to the heavy ion results.

The Optek HES would remain in the output logic high state after transitioning from the logic low state with the solenoid off and no magnetic field present. This behavior was not observed for the output logic high-to-low transition. Instead, the sensor rapidly

switched between states. In comparison, the heavy ion findings observed a toggling of states in both cases and that the magnetic field needed to be re-applied for the device to recover from a transient event. This was also the case for the laser-induced transients.

It was also found that the pulse energy required for the output logic low transition with the solenoid on was considerably higher than that required for the output logic high transition, slightly larger than a factor of four. The difference was considerably higher when comparing the results for the solenoid being off, where the low-to-high transition threshold was 1.075 nJ per pulse and the high-to-low was 20 pJ per pulse. This represents a difference in energy by a factor of about 53. The heavy ion test results reported that the least amount of transient events occurred when the sensor was in the low state with the applied magnetic field [31]. This is in qualitative agreement with the laser findings as out of the four test conditions this state consistently had the highest energy threshold for upset.

In terms of sensitivity to laser pulses, the Infineon HES was found to be more sensitive than the Optek HES when the magnetic field was applied, demonstrating upset at a pulse energy as low as 20 pJ. This is considerably less than the thresholds of 250 pJ and 1.15 nJ shown in Figures 5.7 and 5.9 for the Optek sensor. However, they both demonstrated sensitivity with the field switched off at 20 pJ per pulse.

No single event latchup was observed for the laser power range applied for either sensor. This also agrees with the heavy ion findings in [31][32] and is an important criterion for judging a device's applicability in space missions.

5.10 Conclusions

In comparison to the heavy ion FWHM observations, a lower FWHM for the transient pulses was found for the laser tests. Overall, however, the pulsed laser results obtained for the Optek HES are in good agreement with the data observed for the heavy ion testing. The Infineon HES was more sensitive than the Optek HES when the magnetic field was applied in both test cases, however as mentioned they both showed similar performance when they had no applied magnetic field. This is important as it suggests that a reliable magnet is essential to ensuring their robustness against SETs in a radiation-intensive

environment; without a magnetic field the device may not be able to properly recover to its initial state.

The information provided here on how these devices respond to stimuli when in a high or low state with or without a magnetic field can be useful in the evaluation of their space applicability. The results re-confirm heavy ion data, suggesting that with appropriate mitigation schemes these types of Hall effect sensors can be used in space applications.

5.11 Summary

The Optek and Infineon HESs have been tested using an SPA laser for SEE response. The regions sensitive to laser pulses on both devices were identified. Laser results for the Optek HES have been compared with heavy ion data. As no SEE data was available for the Infineon device the results were compared with the obtained data for the Optek HES. The data obtained for the Optek HES re-confirmed the heavy ion results found by Sanders *et al.*, namely that it is a suitable candidate for space missions with some mitigation schemes.

The results presented here represent the first data obtained for the new setup of the pulsed laser facility at the SSSC using SPA. Thus, these results demonstrate the feasibility of using the SPA method at the pulsed laser facility, as well as the ability to use pulsed lasers to evaluate these types of devices.

Chapter 6
Evaluation of a Xilinx Virtex-5 FPGA Using Two Photon Absorption

6.1 Introduction

Pulsed laser sources have become valuable tools to evaluate the single event effect (SEE) response of electronic devices. In comparison to conventional proton and heavy ion testing, pulsed lasers provide users with considerable spatial and temporal control over irradiation of their devices.

If the incident photon energy of a specific wavelength exceeds the band gap of the material they will be absorbed by single-photon absorption (SPA). While SPA has been used to study SEEs for approximately the past two and a half decades, more recently the study of SEEs via two-photon absorption (TPA) has been demonstrated to be an effective method as well [2]. In TPA, the laser wavelength is specifically chosen so that the photon energy is less than the band gap, thus no optical absorption of individual photons occurs in the material. However, at sufficiently high laser intensities the material can simultaneously absorb two photons and generate an electron-hole pair each time this occurs. Due to its low absorption, TPA has the ability to inject charge at nearly any volume within the device, and as such is useful for backside irradiation of circuits and devices built on silicon wafers.

In this chapter, the results obtained for the single event upset (SEU) evaluation for a commercial off-the-shelf (COTS) Xilinx Virtex-5 field-programmable gate array (FPGA) using the TPA technique are given. Part of the motivation for study is that FPGAs have found widespread applicability in space missions due to their versatility and robustness. In

particular, Xilinx has published several reports that verify the immunity of many Virtex-series FPGAs to single event latchup (SEL) [34][35]. This has made them a preferred choice for space applications.

The primary objectives of this research were to reconfirm the tolerance of the FPGA to SEUs from a pulsed laser source from results previously obtained on the same device at the SSSC pulsed laser facility. This Virtex-5 represents the first device tested using the new equipment setup of the SEE pulsed laser facility at the SSSC, and additionally represents the first device to be tested using the TPA technique. The initial testing was performed by Govindakrishnan Radhakrishnan [36], and the results presented here represent a continuation of this work. The initial results determined the pulse energy thresholds of the various functional blocks present within the FPGA structure, and also determined the cross-section for the configuration memory functional block. Motivation for further study was a result of the laser facility receiving additional upgrades, namely the addition of the Pockels cell into the beamline. At the same time, the ThorImageLS software was also upgraded to version 2.3 so that the Pockels cell could properly interface with the microscope through the user input from the PC. The new features provided by the Pockels cell give considerably more spatial and temporal control over the laser irradiation of a device than was previously possible.

6.2 Device Overview

The device under test (DUT) was a Xilinx Virtex-5 model LX50T FPGA. As its name suggests, the Virtex-5 is the fifth iteration of the Virtex series of FPGAs manufactured by Xilinx, Inc. The Virtex-5 series is manufactured using a 65 nm process and operates with an internal core logic supply voltage of 1.0 V [37]. In particular, the specific DUT tested was mounted on a Digilent Genesys XC5VLX50T-FFG1136 (1C) development board. The board is shown in Figure 6.1 with the Virtex-5 itself in the center.

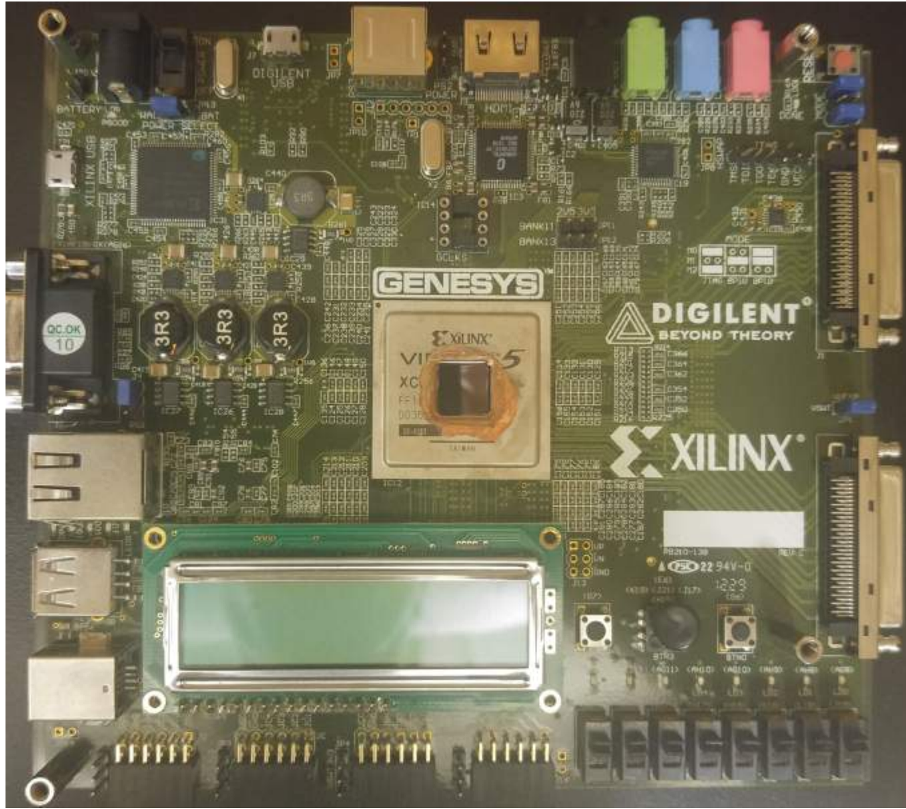

Figure 6.1: Genesys XC5VLX50T-FFG1136 (1C) development board. The Virtex-5 is the component in the center of the board.

The board itself was procured by MDA Corporation in Brampton, Ontario. MDA also supplied the register transfer level (RTL) codes written in the Very High Speed Integrated Circuit hardware description language (VHDL) necessary to operate the various functional blocks inside the FPGA. These codes were slightly modified at the University of Saskatchewan for better suitability for laser testing [36].

As can be seen from Figure 6.1, the metal cover of the Virtex-5 has been etched away in the center to expose the die directly to the pulsed laser. After etching, the silicon surface of the die was polished to a high optical quality to ensure that any incident light from the pulsed or imaging laser is not attenuated by blemishes or imperfections from the etching process. As the Virtex-5 comes in a flip-chip package, this makes it especially suitable for TPA as the backside of the die is exposed to the laser. As a result of the selected wavelength the laser penetrates through the silicon substrate and causes upsets directly via TPA in the diffusion regions of the device. The metal layers do not provide an obstruction in this case as they are located past the substrate and active areas from

the point of view of the laser.

The Virtex-5 die structure is composed of four primary functional blocks: the configuration memory, configurable logic blocks (CLBs), digital signal processing blocks (DSP48E), and block RAM (BRAM) sections. Each of these functional blocks has its own .bit file that must be programmed into the FPGA before beginning any laser test in that area for proper readout of any SEUs (i.e., configuration memory requires the configuration memory .bit file). They are of the most interest for testing of tolerance to SEUs, and are briefly described in their respective experimental sections. The actual locations of the functional blocks within the Virtex-5 were identified previously in [36] using the Xilinx Floorplanner tool to map the information to the geometric layout of the FPGA.

6.3 Experiment Setup

Pulsed laser testing of the Virtex-5 was conducted at the SSSC. The equipment of the facility was previously described in Chapter 4, and a photograph under the microscope is provided in Figure 6.2. Table 6.1 lists the primary laser and equipment parameters used as well as the parameters used in [36] for comparison. To generate the wavelength necessary for TPA, the output beam from the RegA was sent to the OPA 9800. From there the beam was aligned into the Pockels cell before going onwards to the microscope. The ThorLabs PM100 power meter was used to measure the power from the 1200 nm beam directly at the stage. All power measurements were taken in as dark of an environment as possible, however it was noted that the PM100 meter was considerably less sensitive to background light from the room compared to the OP-2 VIS meter used for the Hall effect sensors.

Figure 6.2: Picture of the Virtex-5 development board under the microscope.

Table 6.1: Current and previous laser irradiation parameters for Virtex-5 FPGA studies.

	Current Parameters	**Previous Parameters**
Wavelength (nm)	1200	1200
Objective Lens	10x (NA 0.3), 50x (NA 0.65)	10x (NA 0.3)
Repetition Rate (kHz)	10	1
Pulse Width (fs)	200	200

The notable differences between these two parameter sets are the lenses and the repetition rate. For the configuration memory tests both the 10x and 50x lenses were used while only the 10x was used for the remainder. The repetition rate in the presented testing was also increased to 10 kHz; due to the shorter period it is considerably more favorable for the Pockels cell in terms of the memory required to generate the waveform pattern for laser irradiation. It is also considerably less likely for the Pockels cell to miss pulses due to the asynchronous external signal required by the RegA to reach a 1 kHz repetition rate.

During testing, the Virtex-5 board was connected to a PC so that the FPGA could

be re-programmed with the .bit files for the functional blocks as necessary. This is done using the Xilinx iMPACT software. The board also requires its own power supply. When the device is scanned by the pulsed laser, any disruptions in normal operation can be read back through the JTAG or FPGA debug output lines using iMPACT.

6.4 Configuration Memory Results and Cross Section Correlation with Proton Data

Configuration memory functional blocks compose the majority of the fabric of the Virtex-5. The memory cells within the configuration memory are the fundamental units that store the configuration data for the FPGA. As this data is responsible for determining the functions and interconnects between other FPGA components, the configuration memory functional blocks are often considered the most critical in ensuring the FPGA continues operating normally. Depending on the model, the configuration memory cells of an FPGA can be SRAM-based, flash-based, or antifuse-based [38]. The Virtex-5 is SRAM-based with its memory cells utilizing a modified 6T design [36][39]. Figure 6.3 (a) shows a standard 6T SRAM cell while (b) shows the modified version used in the Virtex-5.

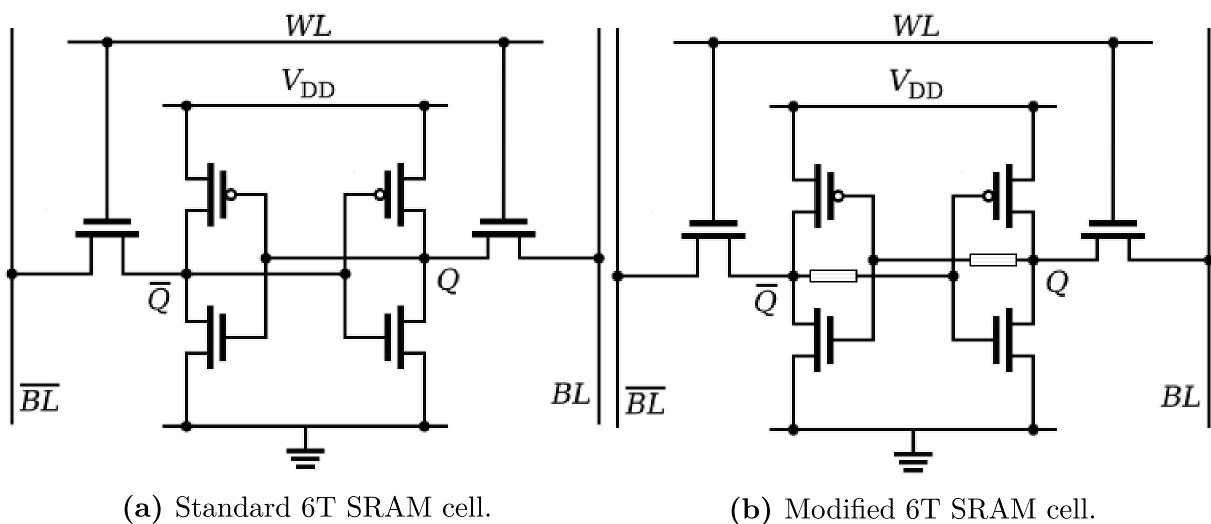

(a) Standard 6T SRAM cell. **(b)** Modified 6T SRAM cell.

Figure 6.3: Standard and modified 6T SRAM cells.

The essential difference between the two is that (b) has added resistance between the cross-coupled inverter connections to increase the feedback time of the cell, thus hardening

it against SEUs to some extent. However, this is not without a drawback as the write time will also increase. Thus this design is not particularly suitable for applications outside of radiation-tolerant memories.

Figure 6.4 shows the view of the repetitive column structure of the configuration memory under the microscope using the imaging laser. As described in Chapters 4 and 5, once again recall that the red areas in the image do not represent sensitive hotspots, but rather simply oversaturation of pixels on the detector connected to the imaging laser.

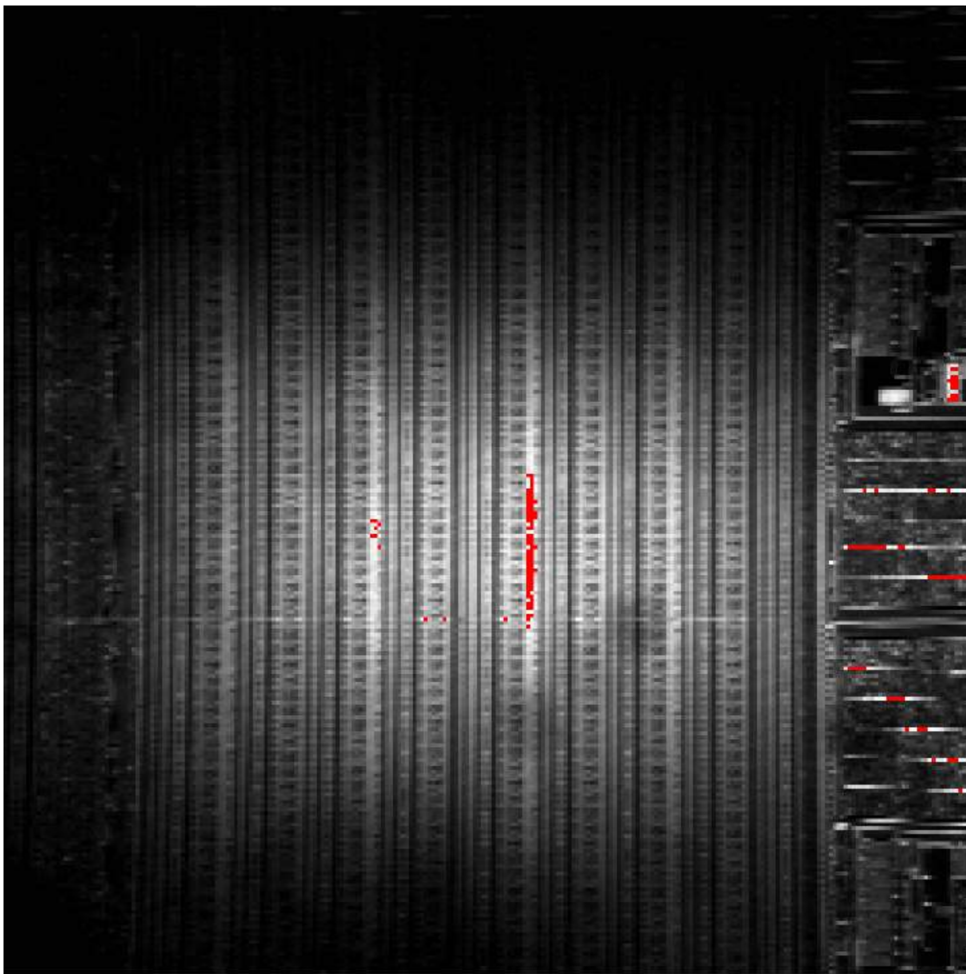

Figure 6.4: Picture of an area of the Virtex-5 configuration memory. The field of view is 1440 μm × 1440 μm. The red regions indicate oversaturation of image pixels on the detector.

For a configuration memory test, the associated .bit file is loaded into the FPGA using iMPACT. The number of resulting errors after a laser irradiation event can be checked by selecting the *Verify* command, which will read out the total number of errors registered

by comparing the original .bit file with the current status.

As the structure of the configuration memory is quite repetitive, a random area was chosen for testing. In this section, the 50x lens was used. Instead of continuously scanning an area under the microscope, a region of interest (ROI) was chosen so that only the area selected would be irradiated by the pulsed laser. The area chosen is shown in Figure 6.5 and parameters selected for the ROI are specified in Table 6.2.

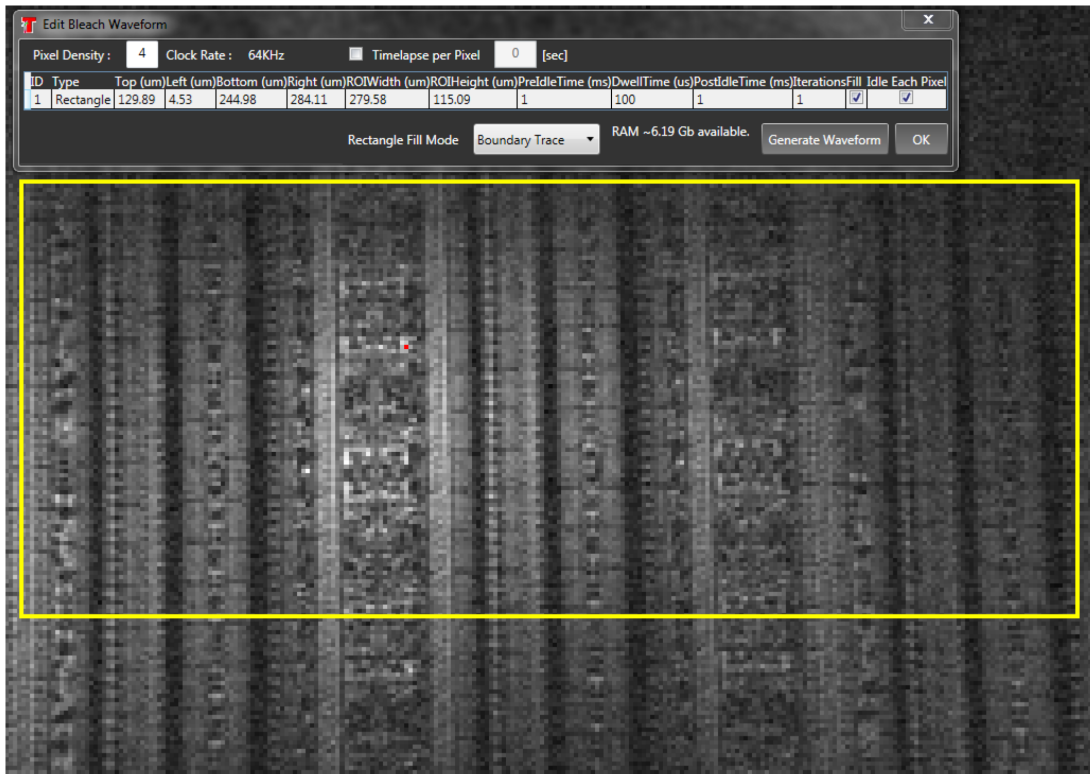

Figure 6.5: Picture of an area of the Virtex-5 configuration memory with a rectangular ROI.

In this configuration, the ROI is scanned along the rectangular boundary of the ROI 200 times. As the length and width dimensions of the ROI are 279 μm and 115.09 μm, the ThorImageLS software converts this into 249 pixels $\times$ 103 pixels. A pixel density of 4 instructs the galvo mirrors to irradiate every 4th pixel in the pattern. The dwell time per pixel is the amount of time the galvo mirrors spend scanning on the pixel. A time of 100 μs is chosen as the repetition rate of the pulsed laser is 10 kHz, thus guaranteeing that each pixel receives exactly one laser pulse. The pre- and post-idle times represent the durations that the galvo mirrors spend on each pixel before and after sending a laser

pulse. During these times the Pockels cell switches off.

Table 6.2: ROI parameters for configuration memory area scan.

Objective Lens	50x (NA 0.65)
Area	$279.59 \times 115.09\ \mu\text{m}^2$
Conversion Factor	1.125 μm/pixel
Pixel Density	4
Dwell Time per Pixel	100 μs
Pre-Idle Time	1 ms
Post-Idle Time	1 ms
Number of Scans	200
Scan Mode	Boundary Trace

Figure 6.6 shows the results obtained for the configuration memory. The rate of error accumulation begins to decelerate at the higher pulse energies. This indicates that the total area exposed to laser pulses is reaching saturation. In other words, the majority of the available memory bits in the area have experienced an error. For this setup, an energy threshold of 330 pJ per pulse was found. No errors below this energy were observed. The energy threshold was previously found to be approximately 300 pJ per pulse [36]. The parameters have been significantly changed between these two tests; as such the threshold values obtained for the pulse energies are in reasonable agreement with the previous data.

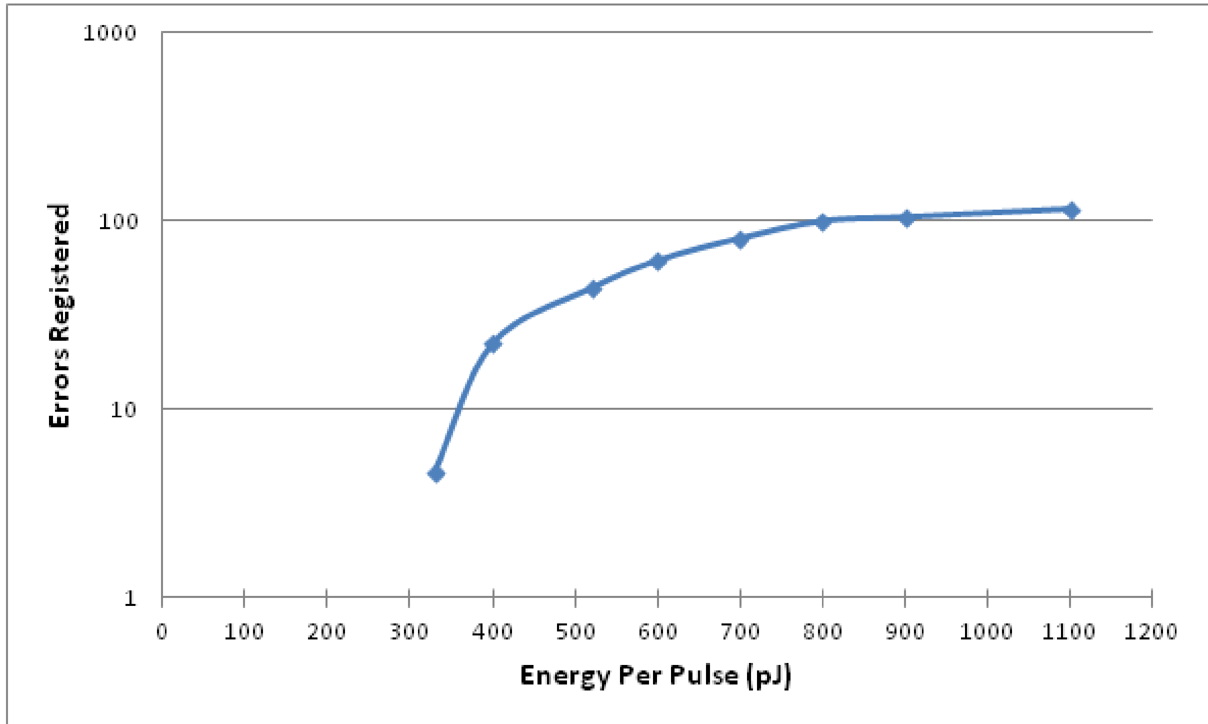

Figure 6.6: Errors experienced by the Virtex-5 configuration memory as a function of laser pulse energy.

6.4.1 Cross Section Comparison with Proton Data

From the parameters used for the data obtained in Figure 6.6 the error cross-section per bit for the configuration memory is calculated and given in Figure 6.7.

SEU response of a Virtex-5 XC5VLX50T model to irradiation by protons was previously evaluated by Hiemstra *et al* [40]. Using a proton beam with energies between 65-120 MeV at TRIUMF, the proton SEU cross section was found to be 1.95×10^{-14} cm^2/bit for the configuration memory of a Virtex-5. Additionally, Quinn *et al.* reported a maximum configuration memory per-bit cross section of 8.61×10^{-14} when a Virtex-5 was exposed to 200 MeV protons [41]. From the data given in Figure 6.7, the lowest obtained cross section value at 330 pJ was found to be 1.74×10^{-12} cm^2/bit. This differs from the obtained proton data by slightly more than an order of magnitude.

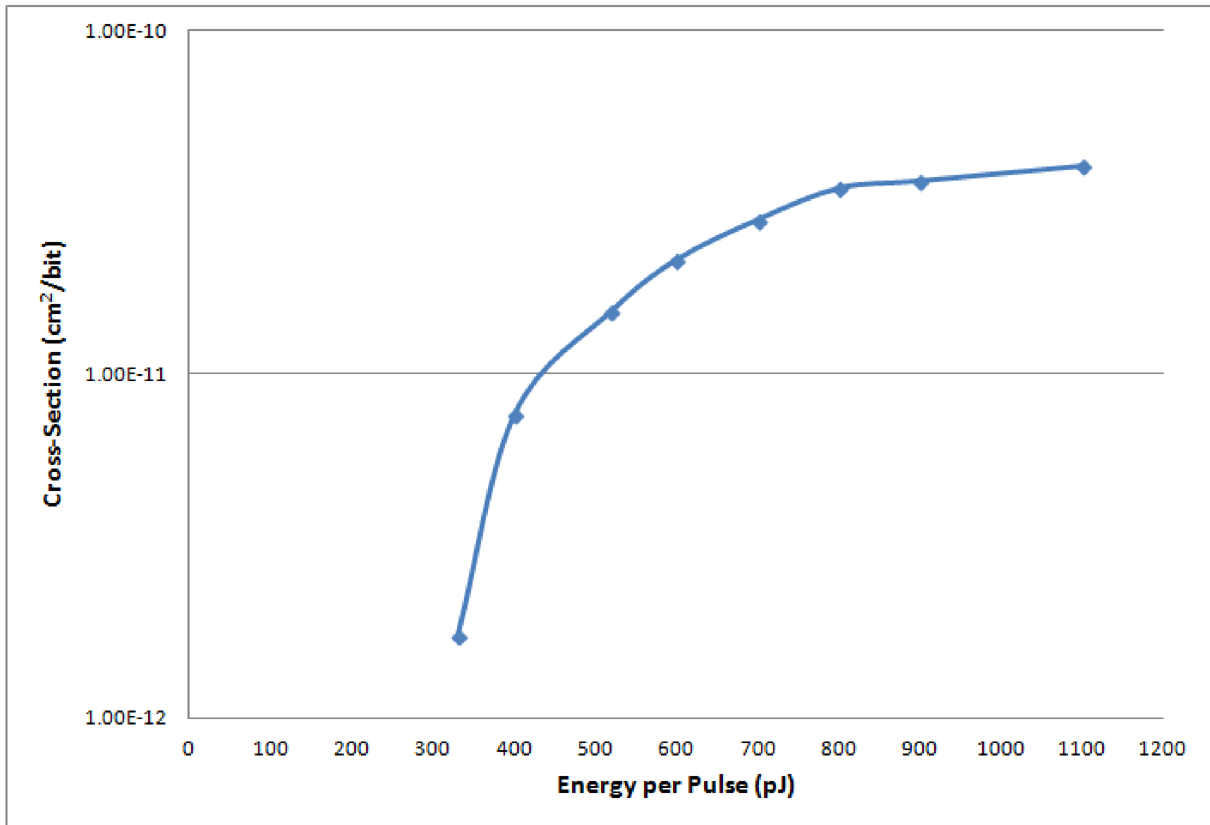

Figure 6.7: Cross section per bit as a function of laser pulse energy of the configuration memory.

As such, it is difficult to quantitatively correlate them. However, while again differing by several orders of magnitude, the trend of the pulsed laser results agrees with the overall trend shown in heavy ion testing. Both methods show the early rapid increase in error accumulation before hitting a saturation point [41].

6.5 Configurable Logic Blocks - Counters

The Virtex-5 contains a set of 456-bit counters distributed throughout the FPGA that use the available configurable logic blocks (CLBs) composed of flip-flops, in contrast to the configuration memory which is SRAM-based. Fortunately, a single counter occupies one column in the FPGA which makes it easier to perform laser testing. Under the microscope the structure looks nearly identical to the configuration memory blocks. However, by using the Xilinx Floorplanner tool the counter locations could be obtained. Figure 6.8 shows the view of the counters under the microscope located near the left edge of the chip.

These were also the counters used for testing. Only 3 of the 4 columns visible in the figure are counters; they are the ones located closest to the input-output block. CLBs are the primary elements used to build combinational and sequential circuits within the FPGA, thus implementing counters in CLBs is useful for SEU evaluation as they utilize the vast majority of their functional logic.

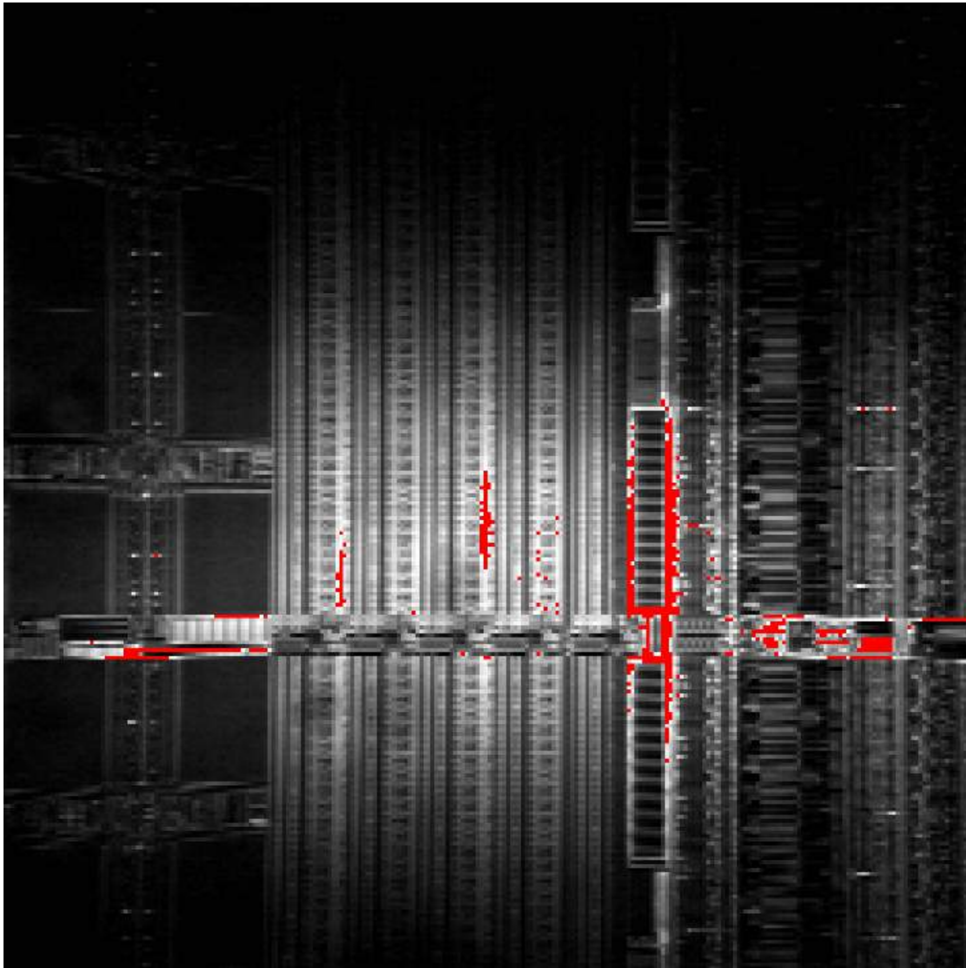

Figure 6.8: The 3 456-bit counter columns as viewed under the microscope. On the left is a BRAM column, while the right side is an input-output block.

For laser scanning, a single column was zoomed in on to ensure that only one column would be hit by laser pulses. Error detection is indicated by any one of 8 green LEDs present on the development board turning on. Specified by the VHDL code, 8 bits of each counter within a section are sent to a comparator to verify their outputs. The output bit from the comparator reports any discrepancies. While each counter contains 456 bits, the 7 least significant bits and most significant bits were chosen for comparison. This was also

specified by the VHDL code, as continuously comparing all 456 bits would be intensive and require a considerably larger comparator instantiation.

Figure 6.9 shows the area used for testing. A single counter was digitally zoomed in to an area of 81 $\times$ 81 μm^2. Two primary testing modes were used: continuous scanning of the entire area with a dwell time of 5.2 μs per pixel and a single point ROI to inject pulses into one specific area in the counter.

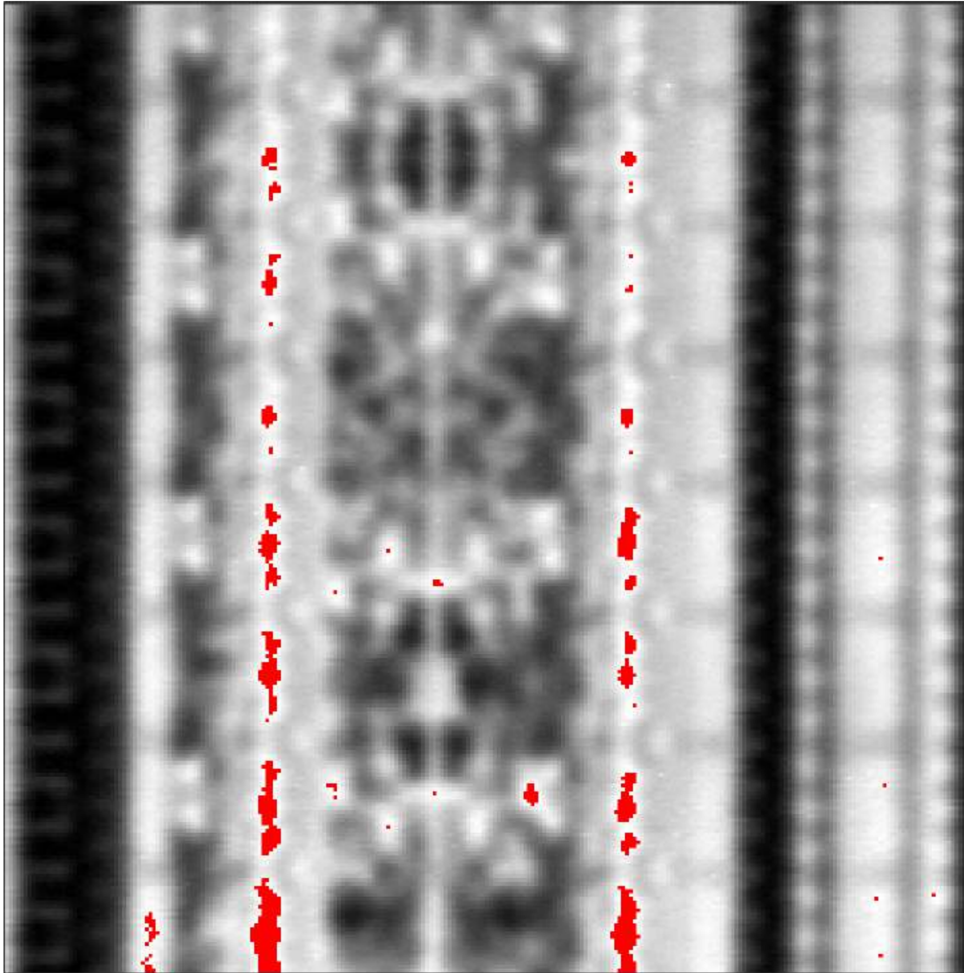

Figure 6.9: 81 x 81 μm^2 view of a single counter column used for pulsed laser testing.

After loading the appropriate .bit file into the FPGA the counter is evaluated for the SEU threshold. In comparison to the configuration memory, the analysis for the counters is slightly more qualitative in that there is no error readout from iMPACT. Instead, the user must monitor the LEDs on the FPGA board during laser irradiation. The instant an LED turns on indicates the first detection of an SEU. Therefore, the metric used to

determine the energy threshold was the time taken between exposing the area to the laser and an LED turning on.

Table 6.3 lists the results of continuously scanning the laser over the area in Figure 6.9.

Table 6.3: Energy threshold test for counter using continuous laser scan mode.

Energy per Pulse (pJ)	**Time before LED Turns on**
450	No light after 10 minute exposure
500	~3 minutes
600	40 seconds
800	Between 4-5 seconds
1000	Instantly

The counters have a higher energy threshold than the configuration memory, which was found to be around 330 pJ per pulse. Here the first SEU indication occurred after approximately 3 minutes at 500 pJ per pulse. The higher tolerance may be due to the CLBs being composed of flip-flops rather than SRAM cells like the configuration memory.

Previous testing of the counters showed a threshold of approximately 700 pJ per pulse [36]. However, the discrepancy may be due to the repetition rate of the laser being increased to 10 kHz from 1 kHz, thus increasing the flux of pulses incident on an area and affecting the charge deposition rate.

A single pulse ROI was also used to evaluate the SEU tolerance. The goal was to observe how many laser pulses in a specific area would be required to generate an error in the counter output. A single point was selected roughly in the center of Figure 6.9 for irradiation. Setting the pixel dwell time to the period of the repetition rate (100 μs) and specifying the number of area scans effectively allows for a custom number of laser pulses to be injected into a single area on the FPGA. Table 6.4 lists the results of using the single point ROI.

Table 6.4: Energy Threshold of CLB Counter for Single Point Region of Interest (ROI) Laser Irradiation

Energy per Pulse (pJ)	Number of Laser Pulses before LED Turns on
1000	90-100
1100	30-40
1200	10

Upset could not be generated under ∼1000 pJ per pulse for 100 pulses or less. Similar to before, this may be due to the flux of the laser pulses. Continuous scanning irradiates a localized area at a much higher rate relative to the single point ROI and therefore may alter the overall charge deposition rate, affecting the probability of experiencing an SEU.

6.6 DSP48 - Multipliers

The Virtex-5 contains a total of 36 DSP48 blocks running in parallel in a single column in the FPGA. Acting as the fundamental units for building multipliers, accumulators, multiplexers, etc., the purpose of the DSP48 blocks is to implement the mathematical functions necessary to perform various DSP (digital signal processing) operations. The multiply and accumulate blocks are arranged in groups of two with each of these being comprised of six DSP blocks chained together. Figure 6.10 shows the DSP48 column located within the FPGA structure, while Figure 6.11 shows the $360 \times 360\ \mu m^2$ area used for laser testing.

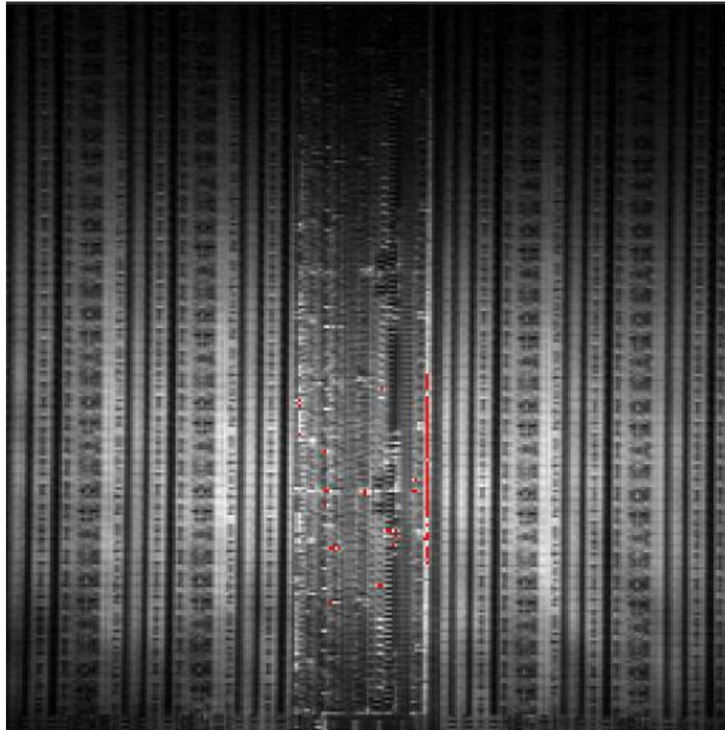

Figure 6.10: DSP48 column located in the center between some configuration memory columns.

Laser testing of the DSP block was quite similar to that of the counters. After programming in the appropriate .bit file, the outputs of the two multiply and accumulate blocks in a group were continuously compared to each other on every clock cycle. If the results did not match, one of the onboard LEDs would turn on in a similar fashion to the counters. Both a continuous scan and single point ROI were used to test the response of the DSP blocks. Table 6.5 lists the results of continuously scanning the ROI in Figure 6.11.

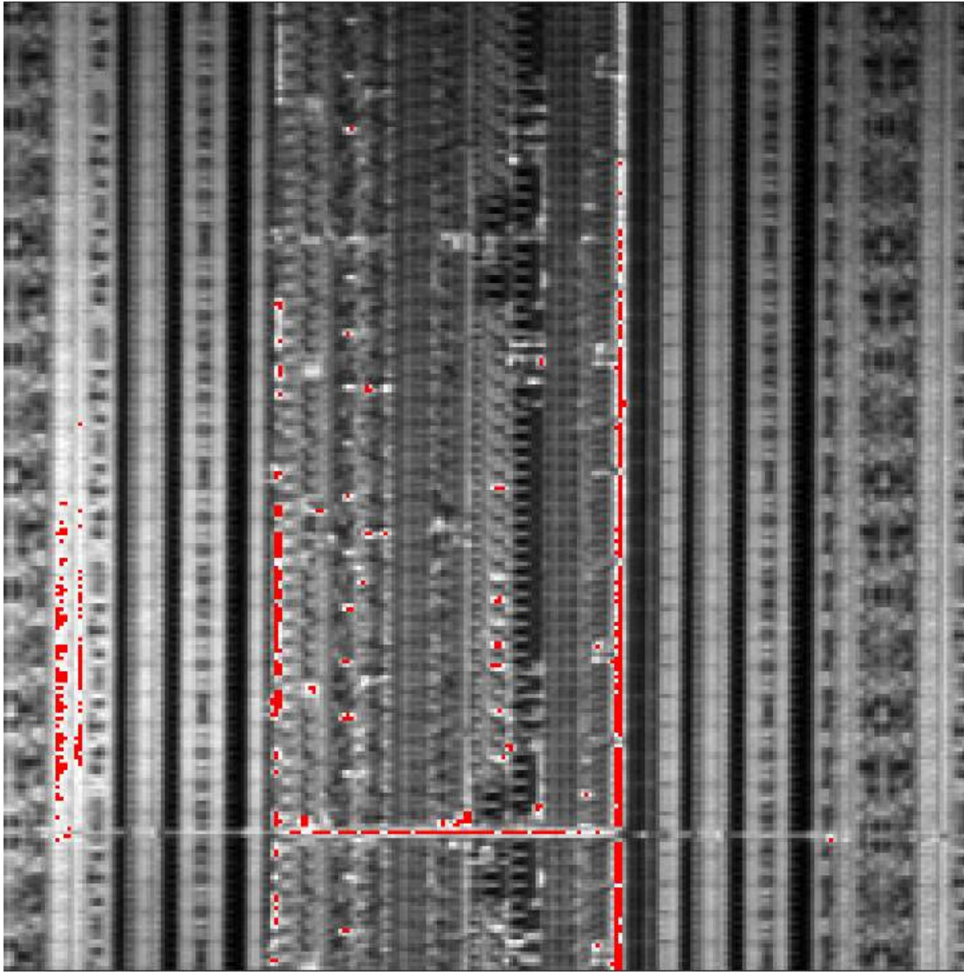

Figure 6.11: DSP48 column located in the center between some configuration memory columns.

Table 6.5: Energy threshold test for DSP block using continuous laser scan mode.

Energy per Pulse (pJ)	Time before LED Turns on
200	No light after 10 minute exposure
300	∼3 minutes
350	20-25 seconds
400	3-6 seconds
450	Instantly-1 second

Table 6.6 lists the results of irradiating a single point on the DSP block with a single point ROI. An area in the center of Figure 6.11 was used.

Table 6.6: Energy threshold of DSP for single point ROI laser irradiation.

Energy per Pulse (pJ)	**Number of Laser Pulses before LED Turns on**
450	60-65
600	30
700	25
800	20
900	15

Using the continuous scan mode the energy threshold was previously found to be between 320-360 pJ per pulse [36]. For this testing it was found to be approximately 300 pJ per pulse. As with the counters, the discrepancy between these values might be explained by the difference in repetition rate between the two experiments.

6.7 Block RAM

Block RAM (BRAM) is used as high density memory in the Virtex-5, composing several columns within the structure distinct from the configuration memory. The VHDL code written for the BRAM works in two modes: read and write. For laser scanning the BRAM must be set to read mode. As data is retrieved from locations in memory additional error detection circuits count the number of bit errors registered. The total errors are summed and read out using the Xilinx ChipScope software, which can then be used to evaluate the BRAM tolerance to SEUs from laser pulses.

Unfortunately, however, for this experiment the BRAM was unable to be tested as the Virtex-5 was previously damaged by the laser as described in the following section. Previous testing showed an energy threshold for the BRAM to be 325 pJ per pulse [36].

6.8 Damage to the Virtex-5

After testing the counter and DSP blocks the configuration memory was tested for single point ROI evaluation. For the single point ROI, the intended goal was to attempt to observe the response at the energy threshold, i.e., the number of detected errors, of the

configuration memory when exposed to single pulses from the laser. Initially, each pulse was generating between 10-20 errors. The average power measured was found to be 2,340 pJ per pulse, approximately twice the threshold of the energies used for previous point ROI threshold testing.

Unfortunately, however, soon after problems were encountered. In an attempt to see if an area of the configuration memory would saturate with errors, a significant permanent error into the Virtex-5 was induced. A single spot in the configuration memory using the point ROI was given a long exposure to the pulsed laser. Setting the software to irradiate the spot for 100 cycles, the spot was exposed to approximately 100 laser pulses localized into a single spot. Figure 6.12 also shows the location where this occurred. Every time the board was reprogrammed and verified without being irradiated by the laser the console would register anywhere from approximately 700 to 1300 errors. Repeated verifications showed considerably inconsistent error messages despite not being exposed to any laser irradiation. Thus, further testing via laser irradiation was compromised as the true errors induced by laser pulses could not be sorted from those generated by an internal failure in the Virtex-5.

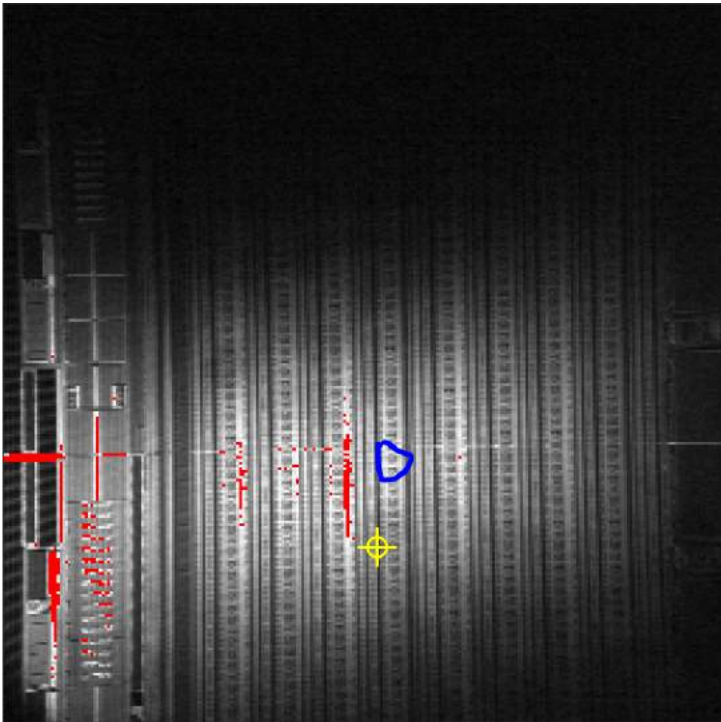

Figure 6.12: Location of permanent damage caused by the laser. The affected area is circled in blue.

Hoping that the board might have recovered some functionality after being given a rest period, re-testing the board several days later yielded the same results.

The permanent error did not only affect the configuration memory despite the error being induced there. Testing for the counters and DSP blocks were also compromised. According to previous testing of the Virtex-5 board, errors in the counter and DSP blocks are indicated through LEDs on the board lighting up. When programming the counter or DSP files into the iMPACT software, the LEDs permanently remained on and thus it could not be seen if pulses from the laser were actually causing upsets in the counter/DSP blocks.

It is unfortunate that while performing testing with the ROI that the permanent error was induced into the Virtex-5 and certainly was not the intention. Care and caution must be taken when testing devices, especially for those with memory cells that can be quite sensitive to laser pulses.

6.9 Discussion

In terms of the pulse energy thresholds, the configuration memory and DSP blocks had similar values of 330 pJ and 300 pJ respectively. However the DSP blocks required a considerable amount of time to experience an upset at that energy as shown in Table 6.5, whereas the configuration memory required only a relatively few scans on the selected ROI. Therefore, the configuration memory blocks are likely to be the most sensitive to SEU in the Virtex-5. This largely agrees with [36] which found the configuration memory to be the most sensitive followed by the BRAM, DSP48, and CLBs/counters. Unfortunately, the information gained when damaging the chip did not provide too useful of a result other than as a future caution for other FPGAs to be tested at the laser facility. As the pulsed laser facility for SEE testing has been set up and gone through several iterations of upgrades, consistency in device testing results is important. With the addition of the Pockels cell and change in standard repetition rate to 10 kHz from 1 kHz, the results obtained for this set of testing and the previous experiment are within acceptable agreement of one another.

The cross section curve previously obtained in [36] for the configuration memory was

shown to be within good agreement with the findings from the proton data in [40] and [41]. However, for the current laser testing the obtained values for the per-bit cross section differed by slightly more than an order of magnitude when compared to the proton data. While this is not in direct agreement with the available data it is important to consider the parameters used for laser irradiation. The high precision and ability to irradiate very specific areas using the new ROI scanning features may affect the probability of generating an error and thus the calculation of the cross section. Even more important to consider is that pulsed lasers and energetic particles differ in their interactions with semiconductor materials. Overall, the current and previous results suggest that the TPA technique developed has potential to emulate the SEUs observed in microelectronics due to particle strikes.

During the course of testing, no SEL was observed to occur on the Virtex-5. The damaging of the chip was not observed to be a latchup event. While not explicitly specified, SEL was not observed for previous testing. Therefore, the TPA laser results reconfirm the assertions by Xilinx and also other groups that reported no observance of SEL in their test setups due to protons and heavy ions.

6.10 Summary

Testing of a Xilinx Virtex-5 FPGA using two photon absorption at the SSSC pulsed laser facility was performed. With the exception of the BRAM, the functional blocks of the FPGA were evaluated for their SEU response. The results presented here were compared to the previous testing performed on the same Virtex-5 to verify both the consistency of the laser setup over time as well as the new upgrades received, namely the Pockels cell. Through this work, the ability of the SSSC pulsed laser facility to test for SEEs using TPA has been demonstrated. With this capability, the facility joins the ranks of a select few locations around the world able to offer TPA laser testing to the radiation effects community and the advantages it brings.

Chapter 7

Summary

The work in this this thesis, the capabilities of the pulsed laser facility at the SSSC to test for SEEs in sensitive devices were described. The testing results of the Hall effect sensors and Virtex-5 FPGA demonstrate the capabilities of the facility to evaluate the SEE response of various devices using both single and twp photon absorption in the same laser setup. More specifically, this work is summarized as follows:

1. Background of single event effects and pulsed lasers.

    - An introduction to single event effects was given, describing the various types and the phenomena they cause in various devices. The particles that cause SEEs, including protons, neutrons, alpha particles, and heavy ions were described.
    - In the succeeding chapter, a brief overview of the fundamentals of laser operations preceded the discussion of the application of pulsed lasers to SEE testing. The phenomena of single and two photon absorption were then discussed and compared in this context. The chapter was concluded with some important parameters to consider when performing pulsed laser testing.

2. Description of the pulsed laser facility at the SSSC.

    - The pulsed laser facility was introduced and described in terms of the equipment used to generate the laser beams for SEE studies. As well, the interaction of the hardware (namely the microscope and Pockels cell) and software combination utilized to give the user even greater precision and control over the spatial and temporal laser irradiation parameters was presented. As nearly

every pulsed laser setup for SEE studies is different, the facility at the SSSC stands to provide some features in unique ways to users wishing to utilize the system.

3. Evaluation of the Hall effect sensors using single photon absorption.

   - The Optek and Infineon Hall effect sensors were evaluated for their response to single event transients using a 580 nm single photon absorption wavelength. Using the laser under the microscope, the most sensitive areas were able to be identified. The transient pulses and their profiles observed for laser testing were in very good agreement with those observed for the available heavy ion data. This testing demonstrated the ability of the pulsed laser facility to test devices for SEEs using single photon absorption.

4. Evaluation of the Virtex-5 FPGA using two photon absorption.

   - The various components of the Virtex-5 FPGA were tested for their response to the 1200 nm two photon absorption wavelength. The goal was to reconfirm previous laser results and compare with proton data on the same Virtex-5 using the new region of interest features available. The results were in good agreement with the previous data with the notable exception of the cross section for the configuration memory. This segment of testing demonstrated the capabilities of the facility using the two photon absorption technique.

Overall, this work contributes to the radiation effects community in two main ways. Firstly, the data obtained from testing the Hall effect sensors and FPGA adds to the database of SEE data available for these devices, and also confirms and correlates within reasonable agreement of available heavy ion and proton data. Secondly, as the SSSC pulsed laser facility has been built up and demonstrated to be capable of evaluating SEEs in different types of microelectronics, it is hoped that it will serve and continue to serve as a location for academic and industrial users to bring their devices for evaluation into the future.

References

[1] Martin A. Green and Mark J. Keevers. Optical properties of intrinsic silicon at 300 k. *Progress in Photovoltaics: Research and Applications*, 3(3):189–192, 1995.

[2] D. McMorrow, W. T. Lotshaw, J. S. Melinger, S. Buchner, and R. L. Pease. Subbandgap laser-induced single event effects: Carrier generation via two-photon absorption. *IEEE Transactions on Nuclear Science*, 49(6):3002–3008, Dec 2002.

[3] Infineon Technologies. Uni- and bipolar hall IC switches for magnetic field applications. http://www.infineon.com/dgdl/Infineon-TLE49X5L-DS-v01_05-en.pdf?fileId=db3a304316f66ee80117549ac8b206b1. Accessed May 2016.

[4] TT Electronics. High reliability Hallogic Hall- effect sensors. http://optekinc.com/datasheets/OMH090.pdf. Accessed May 2016.

[5] G. Moore. Cramming More Components onto Integrated Circuits. *Electronics*, 38(8), April 19, 1965.

[6] D.Hiemstra, MDA Corporation, Brampton, Ontario, Canada. Space Electronics Radiation Effects Course, September 2014. Private Communication.

[7] J. T. Wallmark and S. M. Marcus. Minimum size and maximum packing density of nonredundant semiconductor devices. *Proceedings of the IRE*, 50(3):286–298, March 1962.

[8] D. Binder, E. C. Smith, and A. B. Holman. Satellite anomalies from galactic cosmic rays. *IEEE Transactions on Nuclear Science*, 22(6):2675–2680, Dec 1975.

[9] T. C. May and M. H. Woods. Alpha-particle-induced soft errors in dynamic memories. *IEEE Transactions on Electron Devices*, 26(1):2–9, Jan 1979.

[10] R. Baumann. Soft errors in advanced computer systems. *IEEE Design Test of Computers*, 22(3):258–266, May 2005.

[11] Edward Petersen. *Single Event Effects in Aerospace*. John Wiley & Sons, 2012.

[12] Charles H. Townes. The First Laser. http://www.press.uchicago.edu/Misc/Chicago/284158_townes.html. Accessed April 2016.

[13] Safa O Kasap. *Optoelectronics & Photonics: Principles & Practices: International Edition*. Pearson Higher Ed, 2013.

[14] Karl F Renk. *Basics of Laser Physics: For Students of Science and Engineering.* Springer Science & Business Media, 2012.

[15] L. Krainer, R. Paschotta, S. Lecomte, M. Moser, K. J. Weingarten, and U. Keller. Compact Nd:YVO_4 lasers with pulse repetition rates up to 160 GHz. *IEEE Journal of Quantum Electronics*, 38(10):1331–1338, Oct 2002.

[16] Coherent, Inc. Measuring Laser Power and Energy Output. www.coherent.com/downloads/aboutmeasuringlaserpowerndenergyoutputfinal.pdf. Accessed June 2016.

[17] Coherent, Inc. Lasers: Understanding the Basics. http://www.photonics.com/EDU/Handbook.aspx?AID=25161. Accessed May 2016.

[18] D. H. Habing. The use of lasers to simulate radiation-induced transients in semiconductor devices and circuits. *IEEE Transactions on Nuclear Science*, 12(5):91–100, Oct 1965.

[19] A. K. Richter and I. Arimura. Simulation of heavy charged particle tracks using focused laser beams. *IEEE Transactions on Nuclear Science*, 34(6):1234–1239, Dec 1987.

[20] S. P. Buchner, F. Miller, V. Pouget, and D. P. McMorrow. Pulsed-laser testing for single-event effects investigations. *IEEE Transactions on Nuclear Science*, 60(3):1852–1875, June 2013.

[21] T. Boggess, K. Bohnert, K. Mansour, S. Moss, I. Boyd, and A. Smirl. Simultaneous measurement of the two-photon coefficient and free-carrier cross section above the bandgap of crystalline silicon. *IEEE Journal of Quantum Electronics*, 22(2):360–368, Feb 1986.

[22] Eric W. Van Stryland, H. Vanherzeele, M. A. Woodall, M. J. Soileau, Arthur L. Smirl, Shekhar Guha, and Thomas F. Boggess. Two photon absorption, nonlinear refraction, and optical limiting in semiconductors. *Optical Engineering*, 24(4):244613–244613–, 1985.

[23] Robert W Boyd. *Nonlinear Optics.* Academic press, Apr. 2008.

[24] M. Born and E. Wolf. *Principles of Optics, 7th ed.* Cambridge University Press, Oct. 1999.

[25] Coherent, Inc. *Operator's Manual Vitesse Diode-Pumped, Modelocked Ti:Sapphire Laser*, Santa Clara, CA, 2002.

[26] Coherent, Inc. *Operator's Manual RegA Model 9000 Laser*, Santa Clara, CA, 1997.

[27] Coherent, Inc. *Operator's Manual The Coherent Model 9800/9850 Optical Parametric Amplifier (OPA)*, Santa Clara, CA.

[28] Honeywell. Hall effect sensing and application. http://denethor.wlu.ca/pc300/projects/sensors/hallbook.pdf. Accessed April 2016.

[29] Honeywell. Micropac returns to Mars! Hall effect sensors on Mars Science Laboratory. http://www.micropac.com/images/Other_Documents/MSLCamera_Sensors_08062012.pdf. Accessed April 2016.

[30] R. Phillips, M. Palladino, and C. Courtois. Development of brushed and brushless DC motors for use in the ExoMars drilling and sampling mechanism. *Proceedings of the 41st Aerospace Mechanisms Symposium*, 2012 Jet Propulsion Laboratory.

[31] A.B. Sanders, H.S. Kim, and A Phan. Heavy ion SEE test of OMH3075S Hallogic Hall effects sensor from Optek Technology. http://radhome.gsfc.nasa.gov/radhome/papers/L091906OMH3075S.pdf. Accessed May 2016.

[32] A. B. Sanders, H. S. Kim, and A. Phan. TID and SEE response of Optek Hall effect sensors. In *2008 IEEE Radiation Effects Data Workshop*, pages 148–151, July 2008.

[33] V. Pouget. Facilities and Methods for Radiation Testing Part II - Laser. In *2014 IEEE Nuclear and Space Radiation Effects Conference*, July 2014.

[34] G. M. Swift. Virtex-II static SEU Characterization, Xilinx Radiation Test Consortium, Tech. Rep. 1, 2004.

[35] G.Allen, G.Swift, and C.Carmichael. Virtex-4VQ Static SEU Characterization Summary, Xilinx Radiation Test Consortium, Tech. Rep. 1, 2008 [Online]. Available: http://trs-new.jpl.nasa.gov/dspace/bitstream/2014/40768/1/08-16.pdf. Accessed July 2016.

[36] Govindakrishnan Radhakrishnan. Improved Fault Tolerant SRAM Cell Design & Layout in 130nm Technology. Master's thesis, University of Saskatchewan, Saskatoon, 2014.

[37] Xilinx, Inc. Virtex-5 Family Overview. http://www.xilinx.com/support/documentation/data_sheets/ds100.pdf. Accessed July 2016.

[38] Core Technologies. FPGA Architectures Overview. https://www.pdx.edu/nanogroup/sites/www.pdx.edu.nanogroup/files/FPGA-architecture.pdf. Accessed July 2016.

[39] J. McCollum. Radiation tolerant SRAM bit. Patent application no. US2005/0193255 A1, September 2005.

[40] D. M. Hiemstra, G. Battiston, and P. Gill. Single event upset characterization of the Virtex-5 field programmable gate array using proton irradiation. In *2010 IEEE Radiation Effects Data Workshop*, pages 4–4, July 2010.

[41] H. Quinn, K. Morgan, P. Graham, J. Krone, and M. Caffrey. Static proton and heavy ion testing of the Xilinx Virtex-5 device. In *2007 IEEE Radiation Effects Data Workshop*, volume 0, pages 177–184, July 2007.